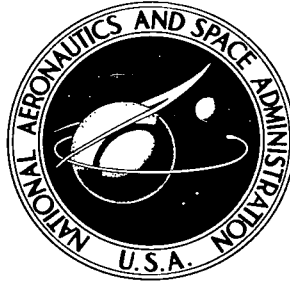


NASA TECHNICAL NOTE



NASA TN D-3519

c. 1

LOAN COPY: RETURN
AFWL (WLIL-2)
KIRTLAND AFB, NM



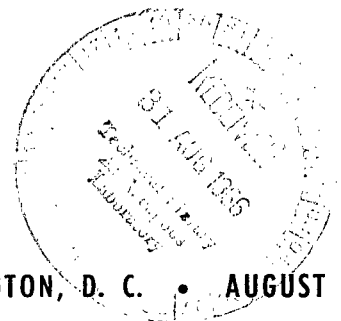
NASA TN D-3519

PRESSURE DRAGS DUE TO TWO-DIMENSIONAL
FABRICATION-TYPE SURFACE ROUGHNESS
ON AN OGIVE CYLINDER AT TRANSONIC SPEEDS

by K. R. Czarnecki and William J. Monta

Langley Research Center

Langley Station, Hampton, Va.





0130335

NASA TN D-3519

PRESSURE DRAGS DUE TO TWO-DIMENSIONAL FABRICATION-TYPE
SURFACE ROUGHNESS ON AN OGIVE CYLINDER
AT TRANSONIC SPEEDS

By K. R. Czarnecki and William J. Monta

Langley Research Center
Langley Station, Hampton, Va.

NATIONAL AERONAUTICS AND SPACE ADMINISTRATION

For sale by the Clearinghouse for Federal Scientific and Technical Information
Springfield, Virginia 22151 - Price \$3.00

PRESSURE DRAGS DUE TO TWO-DIMENSIONAL FABRICATION-TYPE
SURFACE ROUGHNESS ON AN OGIVE CYLINDER
AT TRANSONIC SPEEDS

By K. R. Czarnecki and William J. Monta
Langley Research Center

SUMMARY

An investigation has been made in the transonic Mach number range from 0.70 to 1.20 and over a range of free-stream Reynolds number per foot from about 0.8×10^6 to 6.0×10^6 (2.6×10^6 to 20×10^6 per meter) to determine the pressure drags due to essentially two-dimensional fabrication-type surface roughness immersed in a turbulent boundary layer. Six types of surface roughness, including step, wave, crease, and swept configurations were investigated. The tests were made on an ogive cylinder of fineness ratio 12.2, the roughness elements covering the cylindrical portion of the models. Some data obtained previously on these models at Mach numbers of 1.61 and 2.01 have been included as an aid to the analysis.

The results indicated that at subsonic free-stream Mach numbers all roughness elements had a pressure or form drag. At sufficiently high subsonic and/or supersonic Mach numbers wave drag appeared and became a major component of the total roughness-element drag. The rise in wave drag in the transition from subsonic to supersonic flow was somewhat earlier, more abrupt, and larger in magnitude at the forward stations than at the rearward stations. Sweepback of the roughness elements delayed markedly the onset of compressibility effects and appeared to limit the drag coefficients to lower values than those for the unswept configurations. Effects of Reynolds number per foot (per meter) were usually very small at subsonic speeds and at a maximum when the roughness-element drags were at a maximum at supersonic speeds; decreasing Reynolds number then caused a substantial decrease in drag. Agreement between the experimental drag coefficients and linearized subsonic or supersonic potential-flow theory was poor. Because the ratios of boundary-layer thickness to roughness height for the anticipated range of surface roughness on supersonic transports will most generally correspond to those experienced in this investigation where boundary-layer effects are strong, any accurate estimation of surface roughness drag at transonic and supersonic speeds will require the inclusion of the effects of these ratios.

INTRODUCTION

As part of a program to provide design information for supersonic aircraft, a general investigation is being made at the Langley Research Center to determine the drag of fabrication-type surface roughness in a turbulent boundary layer. Various techniques, including model force tests, roughness-element surface pressure distributions, boundary-layer profile surveys, and schlieren photography, are being utilized in this research. The tests are being conducted in a variety of facilities and over a wide range of operating conditions. Some of the results obtained in this investigation have been presented in references 1 to 5.

Analysis of the aforementioned results disclosed that, at supersonic speeds, the greatest component of drag due to surface roughness in a turbulent boundary layer is contributed by pressure or wave drag. (See refs. 4 and 5.) Theoretical considerations further indicated that this wave drag would be greatest and subject to the most complex Mach-number—boundary-layer interactions near sonic velocity. Consequently, it was deemed desirable to extend the investigation to turbulent boundary layers in the transonic-flow regime. The basic longitudinal pressure distributions and schlieren photographs obtained in these transonic-flow tests have been presented in reference 6. This paper presents the results obtained in integrating the basic pressures to obtain roughness pressure-drag coefficients and relates the drag results with those obtained on the same models at $M = 1.61$ and 2.01 in reference 4.

The pressure-distribution, or pressure-drag, tests were made on six types of fabrication roughness built into the cylindrical portion of an ogive cylinder with a fineness ratio of 12.2 and on a smooth-surface reference model. The tests were made over a Mach number range from 0.70 to 1.20 and over a range of free-stream Reynolds number per foot from about 0.8×10^6 to 6.0×10^6 (2.6×10^6 to 20×10^6 per meter). The model axis was always aligned with the free stream, and turbulent boundary-layer flow was assured by means of a carborundum-grain trip near the tip of the model nose. Where appropriate, a comparison has been made of the experimental pressure-drag coefficients with linearized supersonic theory.

SYMBOLS

Measurements for this investigation were taken in the U.S. Customary Units but are also given parenthetically in the International System of Units (SI). (See ref. 7.)

$C_{D,p}$ roughness-element pressure drag coefficient at a station based on projected roughness frontal area, $\frac{1}{r_{\max}^2 - r_{\min}^2} \int_{r_{\min}^2}^{r_{\max}^2} [(C_p)_{ff} - (C_p)_{rf}] dr^2$

C_p	pressure coefficient, $\frac{p_l - p_\infty}{q_\infty}$
M	Mach number
p	static pressure
p_t	free-stream stagnation pressure
q	dynamic pressure, $0.7\rho M^2$
R	radius of ogive
R/ft (R/m)	free-stream Reynolds number per foot (per meter)
r	model radius measured normal to body axis
x	axial distance from model nose
δ	estimated total boundary-layer thickness
Subscripts:	
l	local conditions just outside the boundary layer
∞	free stream
max	maximum
min	minimum
ff	forward-facing surface
rf	rearward-facing surface

APPARATUS AND METHODS

Wind Tunnel

This investigation was conducted in the Langley 8-foot transonic pressure tunnel, which is a single-return closed-circuit pressure tunnel, capable of operating at stagnation pressures from 0.25 to 2 atmospheres. The Mach number in the slotted test section, which is square, can be continuously varied from 0 to 1.20. The Mach number distribution without a model is reasonably uniform throughout the test-section length of about 5 feet (1.52 m) with the maximum deviation from the average stream Mach number being on the order of ± 0.005 at subsonic speeds to ± 0.02 at the highest test Mach numbers (ref. 8).

Models and Instrumentation

A 50.0-inch-long (127.00 cm), 4.096-inch-diameter (10.40-cm), 3-caliber-nose, ogive cylinder was the basic configuration of the seven sting-mounted models tested. One model was a plain or essentially smooth ogive cylinder without roughness elements. (See fig. 1.) The remaining six models were smooth on the ogive sections, but each had a number of cycles of a particular fabrication roughness constructed into the whole length of the cylindrical portion of the body. (See figs. 2 and 3.) These roughness cycles included steps with grooves, rearward-facing steps, creases, and protruding waves, each having a nearly constant cycle length of from 1.5 to 4.0 inches (3.81 to 10.16 cm) and a constant height of from 0.014 to 0.053 inch (0.036 to 0.135 cm). The heights of the various roughness elements were selected to represent fabrication imperfections found on recent production transonic aircraft of aluminum construction, and the cycle lengths were chosen to provide enough cycles on the models (table I) so that a measurable difference in drag would be obtainable in the related force tests. On four of these models the roughness cycles were wrapped around the model unswept; on the remaining two, they were swept 45° . The relationship of the maximum roughness height to the estimated total boundary-layer thickness (by the method of ref. 9) is shown in figure 4 for $M_\infty = 1.00$. There was little change for the other Mach numbers.

The plain ogive cylinder was constructed of aluminum. The remaining models were made of wood covered with Paraplex and fiber glass. The first 2 inches (5.08 cm) of the nose of each of the fabrication roughness ogive cylinders were aluminum in order to minimize tip damage.

The surface finish of all the models except that of the plain ogive cylinder (which had been slightly roughened for other tests) was very smooth, usually less than 10 micro-inches ($0.25 \mu\text{m}$). Small scale waviness was often present on the models — superimposed on some of the roughness cycles. Although this condition prevented all cycles on any

model from being identical, the deviations from the desired contours were generally few enough and small enough to have no influence upon the conclusions drawn from these tests.

Each model was instrumented with a number of static-pressure orifices (see table II for distances of orifices in terms of r^2) along a generatrix of the model surface. The plain ogive cylinder had 34 orifices. The fabrication roughness ogive cylinders had orifices located along the second and next-to-last cycles of roughness on each model. There were 10 to 18 orifices per cycle with one or two orifices on adjacent cycles for comparison. A greater number of orifices was utilized in this investigation than in that made on the identical roughness models in reference 4, because analysis of the latter results had indicated a need for more adequate surface coverage.

Other instrumentation consisted of a tetrabromoethane (specific gravity of 2.95) manometer board to register model pressures, a 9-inch (22.9-cm) camera to photograph the manometer board, and several precision automatic indicating manometers for measuring reference pressures.

Test Methods

All tests were made at an angle of incidence of 0° with a fully turbulent boundary layer, transition being promoted by No. 60 carborundum grains cemented to the model 0.75 inch (1.9 cm) from the tip. All data were obtained with the tunnel conditions being held in equilibrium. During all runs the dewpoint temperature was maintained low enough to prevent condensation effects.

During the tests a strong effort was made to allow for the inherent lag in the response of the orifice and pressure-tubing system connected to the manometer boards and to insure enough time for the liquid levels on the manometer boards to reach full equilibrium before the boards were photographed. Subsequent evaluation of the data indicated that this objective was not always achieved for all the models at the lowest stagnation pressure of 500 psf (23 940 N/m²) where the lag problem was most severe. In such cases the levels of the pressure distribution curves were too high or too low according to how the test condition was approached. The pressure distributions, however, appeared reasonably accurate and, inasmuch as the effects of erroneous pressure level cancel in the integrations, the drag results should not be too strongly affected and hence have been included in this report.

Range of Tests

Tests were made on each model at Mach numbers of 0.70, 0.90, 1.00, 1.10, and 1.20. Data were taken at nominal stagnation pressures of 3000, 2000, 1000, and 500 pounds per square foot absolute (143 600, 95 800, 47 900, and 23 900 N/m²). The Reynolds numbers

per foot corresponding to these pressures vary with Mach number and range from about 0.8×10^6 to 5.0×10^6 (2.62×10^6 to 16.40×10^6 per meter) at $M_\infty = 0.70$ and from about 1.0×10^6 to 6.0×10^6 (3.28×10^6 to 19.68×10^6 per meter) at $M_\infty = 1.20$. Stagnation temperature was maintained at a value of $120^\circ \pm 2^\circ \text{ F}$ ($322^\circ \pm 1^\circ \text{ K}$) throughout the tests.

RESULTS AND DISCUSSION

Flow Conditions on Smooth Reference Model

The basic flow conditions existing on the smooth-surface reference model can be deduced from the axial pressure distributions determined for the model and presented in figure 5. A solid line has been faired through the average data at each Mach number. The approximate locations of the stations at which pressure distributions were determined over the roughness elements are shown by the braces.

The basic pressure distributions have been discussed in reference 6. The main objectives in presenting these data are to indicate that the forward-station roughness elements are generally located in a regime of more adverse pressure gradient and of higher local Mach number (more negative pressure coefficient), as well as a thinner boundary layer (fig. 4) than the rearward-station roughness elements and that there is shock impingement (of the reflected nose shock) on the cylindrical portion of the model at the low supersonic Mach numbers ($M_\infty = 1.10$ and 1.20) and a recompression shock on the cylinder at $M_\infty = 1.00$ ($x = 24$ in. or 61 cm).

Distribution of Pressure Drag

The distributions of pressures over the roughness elements that were covered in this investigation are presented in figures 6 to 10 in the form of plots of C_p as a function of r^2 for one cycle of roughness. This procedure results in an essentially closed curve wherein the enclosed area is representative of the total pressure drag due to the roughness element, and the differences in C_p between the frontward and rearward sloping faces at constant r^2 are representative of the distribution of pressure drag over the height of the roughness. Usage of r^2 provides for the proper weighting of the larger circumferential distances associated with the upper, or larger, radius portions of the roughness elements when the areas are integrated for total element pressure drag. The drag distributions can be of value in interpreting the importance of various flow effects on roughness drag once the basic flow phenomena are established and allow for some assessment for differences in drag that may be expected for similar roughness elements located on flat plates and on axisymmetric bodies. To establish trends clearly, data are presented for all test Mach numbers and free-stream pressures for the models

with the 0.053-inch (0.135-cm) protruding waves and 0.053-inch (0.135-cm) transverse creases. For all other configurations, because either the trends are similar or the effects of Reynolds number per foot and Mach number are small, the data are restricted to that obtained at the lowest and highest test Mach numbers. No pressure distributions are presented for the model with the 0.021-inch (0.053-cm) steps with grooves inasmuch as no pressures were measured on the step faces and the cylindrical surfaces are parallel to the model axis. Although distribution plots for the model with 0.020-inch (0.051-cm) 45° rearward steps have been included (fig. 9), the presentation required the assumption that the pressures measured immediately behind the step face would apply uniformly over the face. It may be noted that the pressures required for the step face at station 2 on this model were lost in these transonic-flow tests due to irreparable tube malfunction. Also included in figures 6 to 10 are sonic lines which indicate whether the local flow is subsonic or supersonic. These lines were computed by assuming that there were no shock losses involved in the flow over the model.

The pressure-drag distribution data of figures 6 to 10 indicate that, in general, all roughness configurations, whether of the step type involving boundary-layer separation or of the wavy-surface type involving little or no separation, have a pressure or form drag at subsonic speeds. This drag exists even though the local velocities over the roughness elements at no time approach sonic or supersonic speeds. The existence of this pressure or form drag at subsonic flow conditions is believed to be ascribable to two sources: the existence of pressure gradients on the basic body and the growth of the boundary-layer displacement thickness over the length of the roughness element (ref. 10). Pressure gradients, of course, superimpose a basic pressure distribution over the roughness elements which can negate the possibility of obtaining canceling pressures on the forward-facing and rearward-facing surfaces. This effect can be related to the classical buoyancy effect (refs. 11 and 12) of bodies immersed in flows having a static pressure gradient. Favorable pressure gradients generate positive drag and adverse gradients generate negative drag or thrust components on the parts of the roughness elements protruding above the mean surface and the reverse effects exist on the parts indented below the mean surface, the final value of the drag component depending upon the exact shapes of the roughness element and local smooth body pressure distributions. An analysis of the $M_\infty = 0.7$ results for all configurations (figs. 6 to 10) indicates that, for the range of basic-body pressure gradients involved in this investigation, the roughness-drag increments that are believed to be induced by boundary-layer growth over the roughness elements were generally larger than those induced by the buoyancy effects of the basic-body pressure gradients. In general, the effects of basic-body pressure gradients were to increase drag at station 1 and decrease it at station 2 and thus to exaggerate the differences in drag between stations.

At the lowest subsonic test speeds ($M_\infty = 0.70$), the distributions of pressure drag over the heights of the roughness appear to be quite uniform for the model with the 0.053-inch (0.135-cm) protruding waves (fig. 6(a)), but to have a tendency toward concentration near the roots or bases of the roughness elements for the configurations involving creases (part (a) of figs. 7, 8, and 10). Changes in roughness height or sweepback appear to have only a minor effect on this trend. No observation regarding pressure-drag distribution can be made for the step roughness configurations inasmuch as no pressure distributions were measured on the step faces normal to the stream and the assumed pressure distributions may be somewhat in error.

As the free-stream Mach number is increased and the roughness elements penetrate deeper into the supersonic-flow regime (figs. 6 to 10) the pressure drags begin to increase as a result of the generation of supersonic wave drag. Thus, at sufficiently high subsonic speeds and at supersonic speeds the roughness pressure drag is believed to be made up of three components: basic-body pressure-gradient drag, boundary-layer displacement-thickness-growth drag, and wave drag. For the wave-type and crease-type configurations the increase in wave drag first shows up near the top of the roughness element (note the increasing difference in pressure increment between the front and rear roughness surfaces) and then proceeds toward the center height of the element (figs. 6, 7, 8, and 10). At the highest test Mach numbers ($M_\infty = 1.20$) the maximum induced pressure or wave drags occur somewhere between the half and three-quarter height regions of the elements. The increases in drag appear to be somewhat slower for the crease-type configurations than for the wave type and the increases at station 2 are slower than those at station 1. Sweeping the roughness element delays the onset of the increase in pressure or wave drag. (Compare fig. 10 with figs. 6, 7, and 8.) Because of the meager data presented, the Mach number trends for the step-type roughness are not too apparent except for an increasing drag with increasing M_∞ .

Effects of Reynolds number per foot (per meter) on the pressure-drag distributions are generally very small at the subsonic Mach numbers but increase sharply with increasing M_∞ for the unswept wave and crease configurations (figs. 6 to 8) apparently because of the strong influence of the ratio of boundary-layer thickness to roughness height on the development of the local supersonic-flow fields. This thickness ratio increases as the Reynolds number per foot (per meter) decreases and causes the average Mach number in the boundary layer in close proximity to the roughness element to decrease and retard the generation of wave drag. For the sweptback step and crease configurations the effects of Reynolds number per foot (per meter) appear to be relatively small even at the higher test Mach numbers (figs. 9 and 10). A comparison of the results of Mach number and Reynolds number per foot (per meter) in figures 6 and 7 indicates that the effects of increasing Reynolds number per foot (per meter) are similar to the effects of increasing Mach number as was noted in reference 6 in the analysis of

the axial pressure distributions. Similarly, a comparison of drag distributions at station 2 with those of station 1 at constant test conditions indicates trends resembling those of decreasing Reynolds number per foot (per meter) or Mach number. Taken in aggregate, these trends again indicate that the roughness-element drag is probably closely related to the local boundary-layer characteristics and that it may be ultimately possible to correlate the drag increments on this basis and the basic-body pressure gradients.

Pressure-Drag Coefficients

The integrated pressure-drag coefficients are presented in figures 11 to 16 as a function of free-stream Mach number with tunnel stagnation pressure as a parameter and in figures 17 to 22 as a function of free-stream R/ft (R/m) with M_∞ as the parameter. Included in the figures are the experimental results obtained on the identical models (except for detailed orifice distribution) at $M_\infty = 1.61$ and 2.01 (shown in ref. 4 only as average values). Also included in the Mach number plots (figs. 11 to 16) are theoretical curves or bands based on two-dimensional linearized supersonic potential-flow theory and experimental local-flow conditions.

For most configurations the theoretical curves were obtained by making plots of theoretical C_p as a function of r^2 at the test Mach numbers and integrating these plots mechanically. The theoretical C_p 's were obtained from the equation

$$(C_p)_{\text{roughness model}} = (C_p)_{\text{plain model}} + \frac{2(\text{local slope of roughness})}{\sqrt{M_l^2 - 1}} \frac{q_l}{q_\infty}$$

where M_l and q_l are the experimental local Mach number and dynamic pressure just outside the boundary layer on the plain model at about the axial location of the midpoint of the roughness element, and $(C_p)_{\text{plain model}}$ is the experimental pressure-coefficient distribution over the area of interest on the basic, or smooth, model. In essence, the increment in pressure coefficient due to roughness was computed on the basis of the average experimental conditions existing on the smooth body at the element location and this increment was then corrected to free-stream reference conditions. The exact procedure for making the theoretical calculations and justification for use of this approach are presented in reference 4. For Mach numbers other than those for test conditions, the theoretical values were extrapolated by the usual two-dimensional linearized supersonic-flow laws. Inasmuch as the experimental local Mach numbers and pressure-gradient effects (which were small) did not vary in direct proportion to changes in M_∞ a band of values rather than a single curve was obtained. This theoretical approach could not, of course, be applied to the step-type configurations. For these, arbitrary

curves varying inversely as $\sqrt{M_\infty^2 - 1}$ and passing through the highest Mach number and highest stagnation-pressure data for the closest set of orifices were assumed to represent theory. Finally, for the sweptback roughness configurations theoretical curves were also computed by using components of the local flow and surface slope normal to the roughness elements.

Examination of the experimental data plotted against M_∞ (figs. 11 to 16) indicates that, generally, all roughness elements have a form drag at subsonic speeds. This form drag may be small or practically nonexistent if, as at station 2 on the model with 0.014-inch (0.036-cm) 45° creases (fig. 16), the local pressure gradient is adverse and sufficiently strong enough to overcome the effects of boundary-layer growth. As M_∞ is increased wave drag begins to appear and the drag coefficients begin to rise, and finally wave drag becomes the major component of roughness-element drag. For the unswept configurations (figs. 11 to 14) the drag rises are rather abrupt; the drag coefficients reach a maximum and then begin to decrease with further increase in M_∞ . Sweepback of the roughness elements delays markedly the onset of compressibility effects and appears to limit the maximum drag coefficients to lower values than for the unswept case. (Compare figs. 11 to 14 with figs. 15 and 16.) These basic trends are in agreement with those expected for bodies tested in a uniform stream of air or outside of a boundary layer.

The drag rises also generally occur somewhat earlier and are more abrupt and larger in magnitude at the forward stations than at the rearward stations. These trends are due to the smaller ratios of boundary-layer thickness to roughness height existing at the forward stations.

It may be noted that the data for station 2 on the model with 0.053-inch (0.135-cm) protruding waves (fig. 12) and to a lesser extent the data for the same station on the model with 0.053-inch (0.135-cm) transverse creases (fig. 13) indicate a tendency toward a dip in the drag curve at $M_\infty = 1.20$. This tendency results from the fact that the model nose shock is reflected back onto the model in the vicinity of the rearward portions of the roughness elements at this station (fig. 5) and creates a favorable interference effect. The interference effect need not be favorable inasmuch as it depends upon what portion of the roughness surface the shock impinges. The interference effect is present but is less discernible on the other models at this test Mach number. Inasmuch as the basic flow fields can be distorted for some distance downstream of the point of shock impingement (fig. 5), and in these tests the shock is reflected onto the model at all supersonic free-stream Mach numbers, it becomes apparent that the drag data within this Mach number region at station 2 are probably not exactly representative of those that would be obtained in interference-free flight. It is believed, however, that the major trends will

not be altered significantly and that the interaction effects will not unduly hinder analysis of the drag in terms of local conditions.

Effects of Reynolds number per foot (per meter) were usually very small at subsonic speeds and were at a maximum when the roughness-element drags were at a maximum at supersonic speeds (figs. 11 to 16); when roughness-element drags were at a maximum decreasing Reynolds number caused a substantial decrease in drag. As was pointed out in reference 6 and in the previous discussion of drag distribution in this paper, this trend derives directly from the influence of Reynolds number on the ratio of boundary-layer thickness to roughness height which then influences the development of the supersonic flow over the roughness element. For the configuration with the 0.021-inch (0.053-cm) steps with grooves, data are presented for two sets of surface orifices close to the step faces normal to the model axis. The data based on the original orifices closest to the step faces (fig. 11(a)) are intended primarily to show Mach number effects inasmuch as no data were available at $M_\infty = 1.61$ and 2.01 for the newer and closer orifices. The data from the newer set of orifices (fig. 11(b)) is believed, however, to present the more correct picture of effects of Reynolds number per foot (per meter) because of the probable proximity of the older set to the points of flow separation or reattachment (ref. 4).

The effects of changes in Reynolds number per foot (per meter) can be seen more distinctly in figures 17 to 22. These figures show that there is little effect of R/ft (R/m) at subsonic speeds, and there is a tendency toward an increase in form drag at the lowest values of R/ft (R/m). This tendency is in accordance with the theoretical expectation that the faster rate of growth of boundary-layer displacement thickness over the length of roughness element at the lower values of R/ft (R/m) will lead to greater form drag. The greatest effects of Reynolds number per foot (per meter) occur at supersonic speeds and when the roughness drag coefficients (wave drags) are highest. The apparent lack of effects of R/ft (R/m) at $M_\infty = 1.61$ and 2.01 at station 2 on the model with the 0.017-inch (0.043-cm) transverse creases should be discounted because of inadequate surface pressure coverage. It should be noted that the ratios of boundary-layer thickness to roughness height for the anticipated range of surface roughness on supersonic transports will most generally correspond to those experienced at the lowest R/ft (R/m) in this investigation where boundary-layer effects are strong. Consequently, the conclusion can be made that any accurate estimation of surface roughness pressure drag at transonic and supersonic speeds will require the inclusion of effects of boundary-layer thickness to roughness height.

At subsonic speeds (figs. 11 to 16), potential-flow theory which does not account for boundary-layer growth does not predict any drag for the roughness elements exclusive of the basic pressure-gradient effects which were generally smaller than the viscous flow

effects. Agreement of experiment with subsonic potential-flow theory hence can be said to be poor. Examination of the data for supersonic speeds, where wave drag is theoretically predicted, indicates that the agreement of experiment with theory is also poor. At the lower supersonic Mach numbers the disagreement stems from the inadequacy of any supersonic theory in a transonic-flow regime, from neglect of the changes in effective roughness shape due to the longitudinal growth of the boundary-layer displacement thickness, and from neglect of the fact that deep within the boundary layer the effective Mach number influencing the wave-drag characteristics of the roughness elements is much smaller than the free-stream value. At the higher supersonic test speeds the first defect should be of negligible importance except for the swept roughness configurations, but the second and third defects should increase in importance inasmuch as the development of the supersonic flow is influenced over a longer region.

In addition to the items just discussed, a more detailed examination reveals that although the pressure-gradient effects generally tend to increase the experimental pressure drag at the forward stations as compared with that at the rearward stations, the effects are relatively small. Further, even though the effects of the rate of growth of displacement-thickness alone are to generate higher pressure or form drags at the forward stations, analysis indicates that the effects are again relatively small. Thus the strong trend toward lower total pressure drags at the rearward stations suggests that the main item contributing to the discrepancy between theory and experiment at supersonic Mach numbers is related to the ratio of the roughness height to the boundary-layer thickness. A preliminary analysis indicates that the effects of the ratio of the roughness height to the boundary-layer thickness become more and more important as the wave length of the roughness elements decreases to, and becomes less than, the thickness of the boundary layer at the roughness elements.

Finally, for the unswept configurations, the experimental drag coefficients of the roughness elements decrease with increasing Mach number at constant Reynolds number per foot (per meter) and sufficiently high Mach number, approximately as indicated by theory.

CONCLUSIONS

An investigation has been made in the transonic Mach number range from 0.70 to 1.20 and over a free-stream Reynolds number per foot from about 0.8×10^6 to 6.0×10^6 (2.6×10^6 to 20×10^6 per meter) to determine the pressure drags due to two-dimensional fabrication-type surface roughness. The results indicate the following conclusions:

1. At subsonic free-stream Mach numbers all roughness elements have a pressure or form drag which is believed to be derived from both basic-body pressure-gradient

effects and the growth in boundary-layer displacement thickness over the length of the element.

2. At sufficiently high subsonic and/or supersonic free-stream Mach numbers, wave drag appeared and became the major component of the roughness-element drag.

3. The rise in wave drag in the transition from subsonic to supersonic flow occurred somewhat earlier and was more abrupt and larger in magnitude at the forward stations where the ratio of the boundary-layer thickness to roughness height was less than at the rearward stations.

4. Sweepback of the roughness elements delayed markedly the onset of compressibility effects and appeared to limit the drag coefficients to lower values than for the unswept configurations.

5. Effects of Reynolds number per foot (per meter) were usually very small at subsonic speeds and were at a maximum when the roughness-element drags were at a maximum at supersonic speeds; when roughness-element drags were at a maximum, decreasing Reynolds number caused a substantial decrease in drag.

6. Agreement between the experimental roughness-element drag coefficients and linearized potential-flow theory was poor at both subsonic and supersonic speeds because of the neglect of the effective changes in roughness shape due to boundary-layer displacement-thickness growth. At low supersonic Mach numbers the disagreement is also partly due to the inadequacy of a supersonic theory in a transonic-flow regime and to the neglect of the fact that deep within the boundary layer the effective Mach number influencing the wave-drag characteristics of the roughness elements is much smaller than the free-stream value.

7. Because the ratios of boundary-layer thickness to roughness height for the anticipated range of surface roughness on supersonic transports will most generally correspond to those experienced at the lowest Reynolds number per foot (per meter) in this investigation where boundary-layer effects are strong, any accurate estimation of surface roughness drag at transonic and supersonic speeds will require the inclusion of the effects of these ratios.

Langley Research Center,
National Aeronautics and Space Administration,
Langley Station, Hampton, Va., March 9, 1966.

REFERENCES

1. Czarnecki, K. R.; Robinson, Ross B.; and Hilton, John H., Jr.: Investigation of Distributed Surface Roughness on a Body of Revolution at a Mach Number of 1.61. NACA TN 3230, 1954.
2. Sevier, John R., Jr.; and Czarnecki, K. R.: Investigation of Effects of Distributed Surface Roughness on a Turbulent Boundary Layer Over a Body of Revolution at a Mach Number of 2.01. NACA TN 4183, 1958.
3. Czarnecki, K. R.; Sevier, John R., Jr.; and Carmel, Melvin M.: Effects of Fabrication-Type Roughness on Turbulent Skin Friction at Supersonic Speeds. NACA TN 4299, 1958.
4. Czarnecki, K. R.; and Monta, William J.: Pressure Distributions and Wave Drag Due to Two-Dimensional Fabrication-Type Surface Roughness on an Ogive Cylinder at Mach Numbers of 1.61 and 2.01. NASA TN D-835, 1961.
5. Czarnecki, K. R.; and Monta, William J.: Boundary-Layer Velocity Profiles and Skin Friction Due to Surface Roughness on an Ogive Cylinder at Mach Numbers of 1.61 and 2.01. NASA TN D-2048, 1963.
6. Czarnecki, K. R.; and Monta, William J.: Pressure Distributions Due to Two-Dimensional Fabrication-Type Surface Roughness on an Ogive Cylinder at Transonic Speeds. NASA TN D-3516, 1966.
7. Mechtly, E. A.: The International System of Units - Physical Constants and Conversion Factors. NASA SP-7012, 1964.
8. Mugler, John P., Jr.: Transonic Wind-Tunnel Investigation of the Aerodynamic Loading Characteristics of a 60° Delta Wing in the Presence of a Body With and Without Indentation. NACA RM L55G11, 1955.
9. Tucker, Maurice: Approximate Calculation of Turbulent Boundary-Layer Development in Compressible Flow. NACA TN 2337, 1951.
10. Schlichting, Hermann (J. Kestin, trans.): Boundary Layer Theory. McGraw-Hill Book Co., Inc., 1955, p. 477.
11. Pope, Alan: Wind-Tunnel Testing. Second ed., John Wiley & Sons, Inc., c.1954, pp. 268-344.
12. Hasel, Lowell E.; Sinclair, Archibald R.; and Hamilton, Clyde V.: Preliminary Investigation of the Drag Characteristics of the NACA RM-10 Missile at Mach Numbers of 1.40 and 1.59 in the Langley 4- by 4-Foot Supersonic Tunnel. NACA RM L52A14, 1952.

TABLE I.- MODEL DESIGNATIONS

Model	Designations	Number of cycles of roughness
1	85 microinches (2.2 μm)	- - - - -
2	0.021-inch (0.053-cm) steps with grooves	9
3	0.053-inch (0.135-cm) protruding waves	24
4	0.053-inch (0.135-cm) transverse creases	24
5	0.017-inch (0.043-cm) transverse creases	24
6	0.020-inch (0.051-cm) 45 ⁰ rearward steps	5 stripes
7	0.014-inch (0.036-cm) 45 ⁰ creases	6 stripes

TABLE II.- MODEL ORIFICE LOCATIONS

Orifice	x, in., for model 1	Orifice	r ² , in ² , for model -			
			3	4	5	7
		Station 1				
1	1.01	1	4.339	4.140	4.134	4.175
2	1.95	2	4.402	4.131	4.136	4.176
3	2.82	3	4.372	4.098	4.132	4.171
4	3.81	4	4.301	4.056	4.125	4.162
5	4.78	5	4.246	4.012	4.118	4.151
6	5.78	6	4.211	3.964	4.105	4.133
7	6.76	7	4.198	3.924	4.084	4.113
8	7.76	8	4.190	3.907	4.063	4.101
9	8.77	9	4.190	3.976	4.080	4.121
10	9.79	10	4.198	4.036	4.097	4.137
11	10.78	11	4.221	4.069	4.115	4.149
12	11.80	12	4.285	4.113	4.125	4.162
13	12.78	13	4.347	4.129	4.131	4.167
14	13.77	14	4.408	4.148	4.131	4.175
15	14.78	15	4.368	4.146	4.129	4.184
16	15.78	Station 2				
17	16.78	16	4.356	4.156	4.142	4.271
18	17.75	17	4.410	4.155	4.139	4.269
19	18.79	18	4.372	4.147	4.130	4.260
20	19.78	19	4.306	4.125	4.121	4.252
21	20.78	20	4.248	4.088	4.114	4.242
22	22.75	21	4.207	4.036	4.101	4.227
23	24.74	22	4.198	3.988	4.088	4.215
24	26.77	23	4.186	3.958	4.081	4.206
25	28.76	24	4.198	4.024	4.092	4.219
26	30.77	25	4.207	4.060	4.105	4.231
27	32.76	26	4.223	4.118	4.120	4.246
28	34.78	27	4.277	4.137	4.129	4.256
29	36.79	28	4.335	4.148	4.132	4.265
30	42.14	29	4.412	4.195	4.142	4.269
31	44.10	30	4.389	4.154	4.145	4.270
32	46.08					
33	48.08					
34	49.62					

Orifice	r ² , in ² , for model 6	Station 1	
		1	2
1	4.052	1	4.052
2	4.060	2	4.060
3	4.068	3	4.068
4	4.072	4	4.072
5	4.076	5	4.076
6	4.078	6	4.078
7	4.080	7	4.080
8	4.080	8	4.080
9	4.084	9	4.084
10	4.095	10	4.095
11	4.097	11	4.097
12	4.006	12	4.006
Station 2			
13	3.960	13	3.960
14	3.972	14	3.972
15	3.987	15	3.987
16	4.004	16	4.004
17	4.018	17	4.018
18	4.028	18	4.028
19	4.030	19	4.030
20	4.022	20	4.022
21	4.032	21	4.032
22	4.046	22	4.046
23	4.048	23	4.048
24	4.005	24	4.005

Orifice	x, cm, for model 1	Orifice	r ² , cm ² , for model -			
			3	4	5	7
		Station 1				
1	2.57	1	27.99	26.71	26.67	26.94
2	4.95	2	28.40	26.65	26.68	26.94
3	7.16	3	28.21	26.44	26.66	26.91
4	9.68	4	27.75	26.17	26.61	26.85
5	12.14	5	27.39	25.88	26.57	26.78
6	14.68	6	27.17	25.57	26.48	26.66
7	17.17	7	27.08	25.32	26.35	26.54
8	19.71	8	27.03	25.21	26.12	26.46
9	22.28	9	27.03	25.65	26.32	26.59
10	24.87	10	27.08	26.04	26.43	26.69
11	27.38	11	27.23	26.25	26.55	26.77
12	29.97	12	27.65	26.54	26.61	26.85
13	32.46	13	28.05	26.64	26.65	26.88
14	34.98	14	28.44	26.76	26.65	26.94
15	37.54	15	28.18	26.75	26.64	26.99
Station 2						
16	45.09	16	28.10	26.81	26.72	27.55
17	47.73	17	28.45	26.81	26.70	27.54
18	50.24	18	28.21	26.75	26.65	27.48
19	52.78	19	27.78	26.61	26.59	27.43
20	57.78	20	27.41	26.37	26.54	27.37
21	62.84	21	27.14	26.04	26.46	27.27
22	68.00	22	27.08	25.73	26.37	27.19
23	73.05	23	27.00	25.54	26.33	27.14
24	78.16	24	27.08	25.96	26.40	27.22
25	83.21	25	27.14	26.19	26.48	27.30
26	88.34	26	27.25	26.57	26.58	27.39
27	93.45	27	27.59	26.69	26.64	27.46
28	107.04	28	27.97	26.76	26.66	27.52
29	112.01	29	28.46	27.06	26.72	27.54
30	117.04	30	28.32	26.80	26.74	27.55
31	122.12					
32	122.12					
33	122.12					
34	126.03					

Orifice	r ² , cm ² , for model 6	Station 1	
		1	2
1	26.14	1	26.14
2	26.19	2	26.19
3	26.25	3	26.25
4	26.27	4	26.27
5	26.30	5	26.30
6	26.31	6	26.31
7	26.32	7	26.32
8	26.32	8	26.32
9	26.35	9	26.35
10	26.42	10	26.42
11	26.43	11	26.43
12	25.85	12	25.85
Station 2			
13	25.55	13	25.55
14	25.63	14	25.63
15	25.72	15	25.72
16	25.83	16	25.83
17	25.92	17	25.92
18	25.99	18	25.99
19	26.00	19	26.00
20	25.95	20	25.95
21	26.01	21	26.01
22	26.10	22	26.10
23	26.12	23	26.12
24	25.84	24	25.84

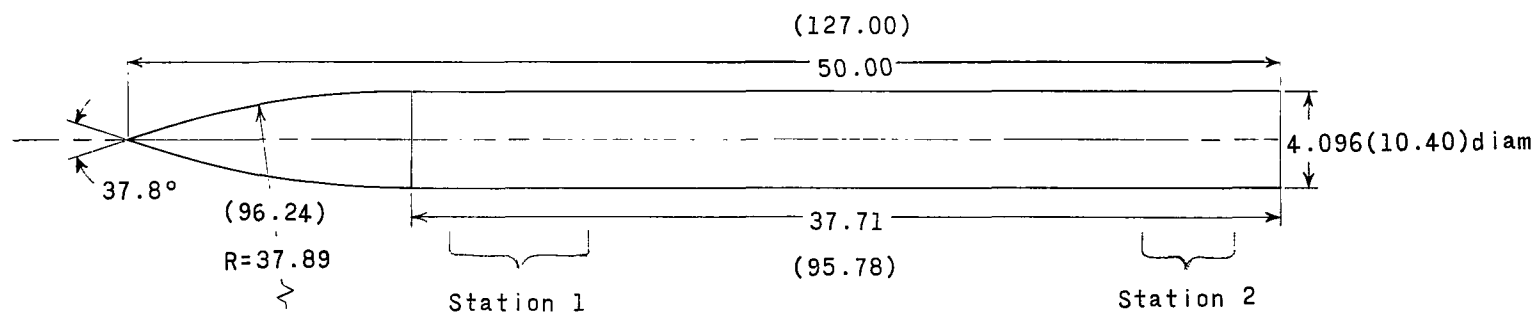
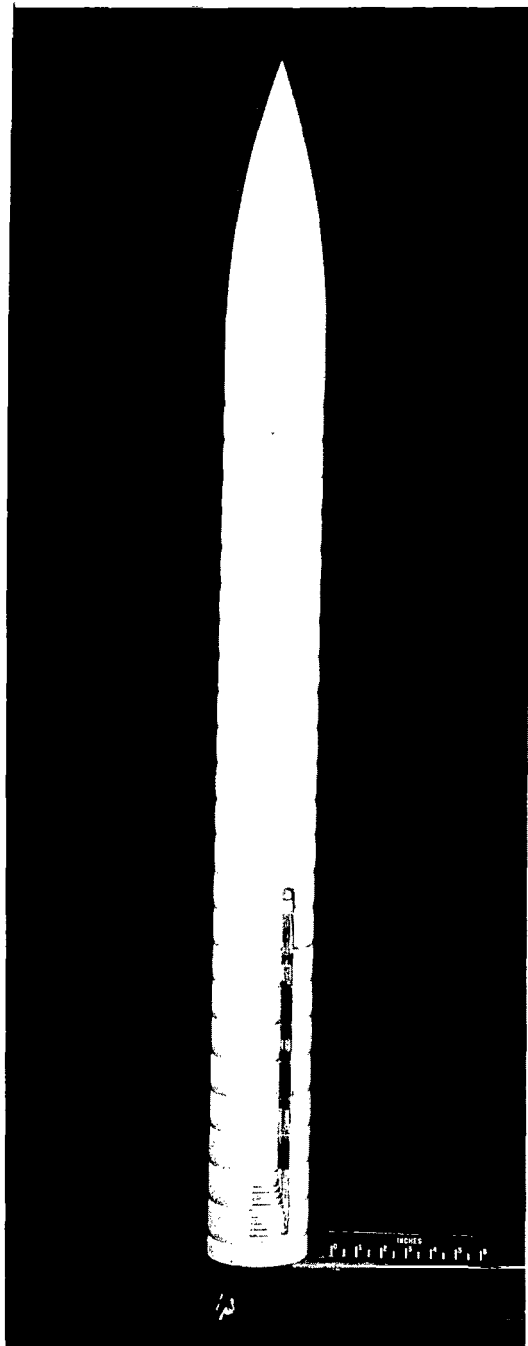
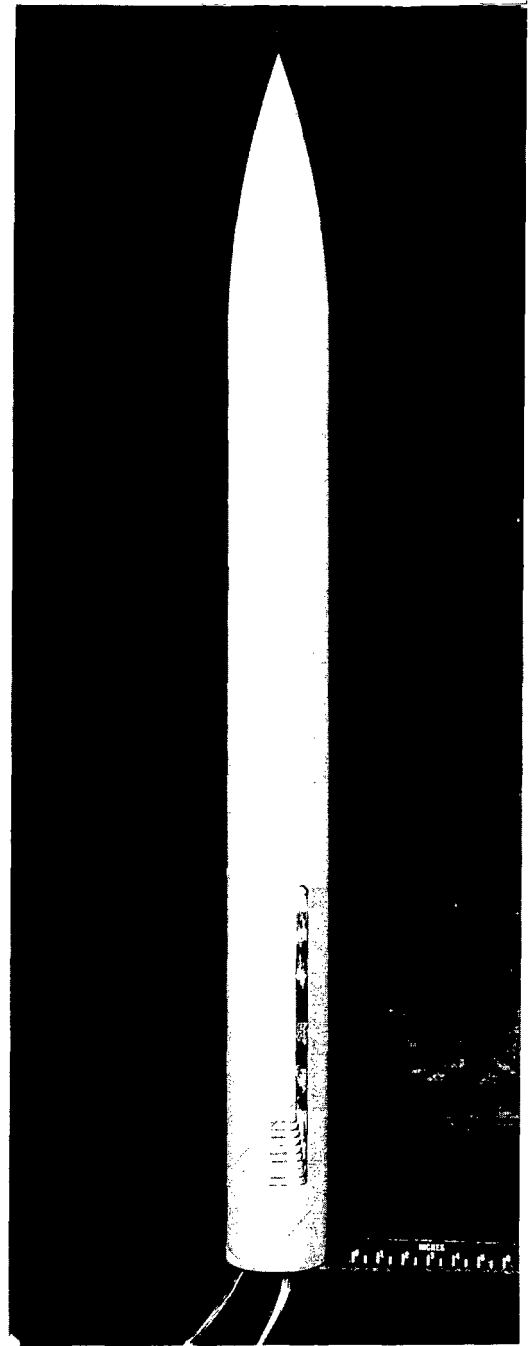


Figure 1- Sketch of basic model. All dimensions are in inches (centimeters in parentheses) unless otherwise stated.



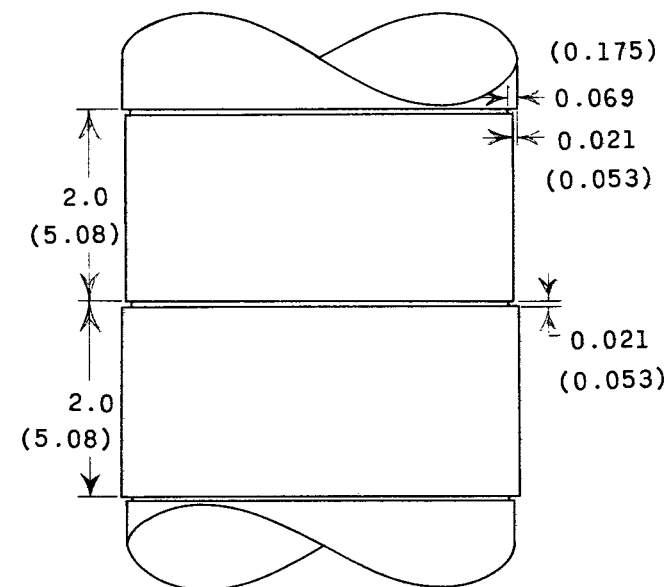
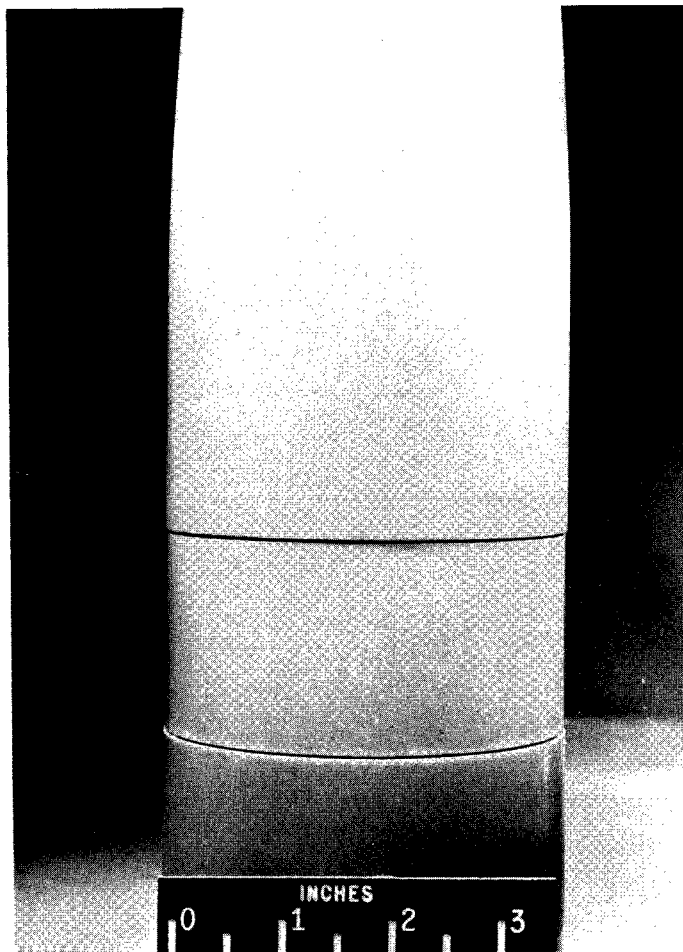
(a) 0.053-inch (0.135-cm) transverse creases.



(b) 0.020-inch (0.051-cm) 45° rearward steps.

Figure 2.- Photographs of typical roughness models.

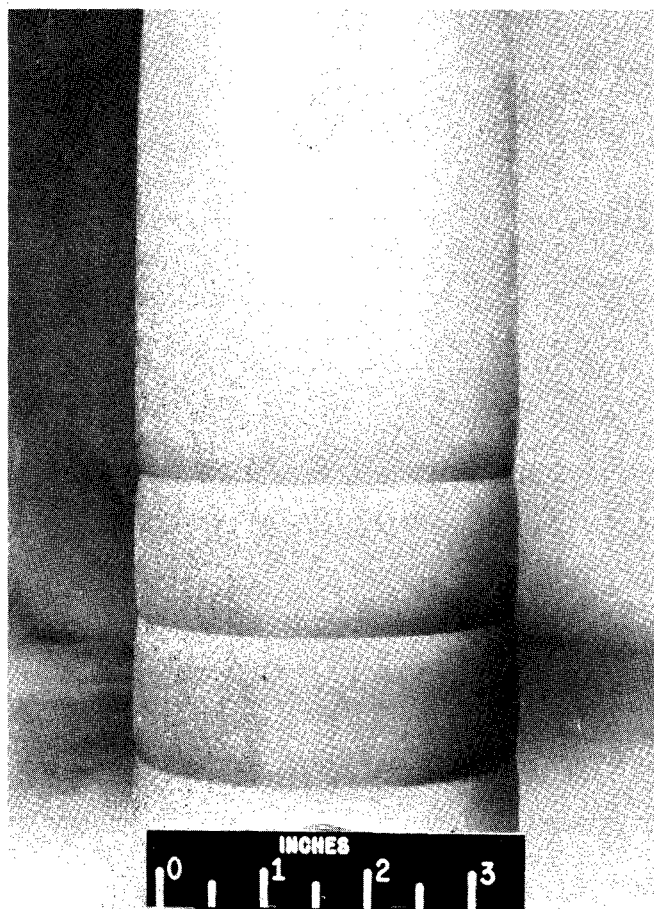
L-61-1039



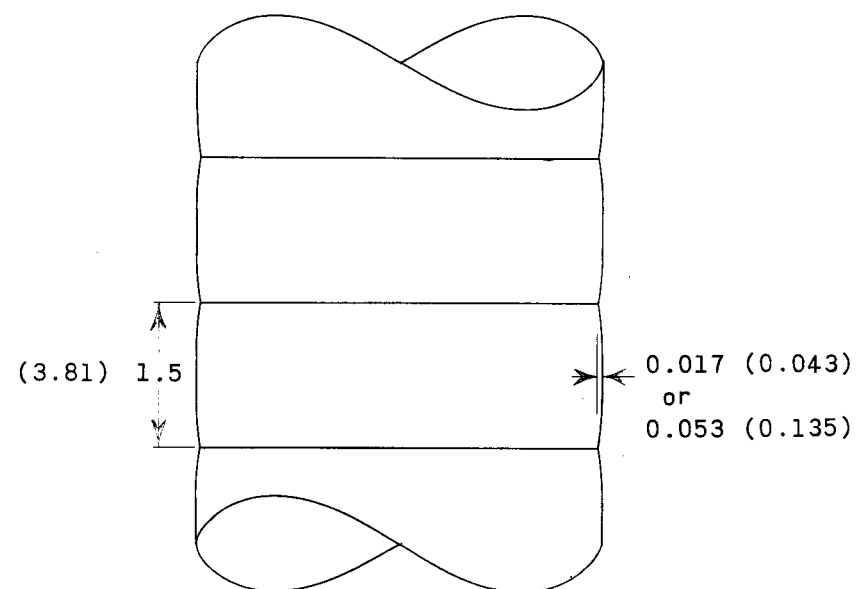
(a) 0.021-inch (0.053-cm) steps with grooves.

L-61-1040

Figure 3.- Details of fabrication-type roughness. All dimensions are in inches (centimeters in parentheses) unless otherwise stated.

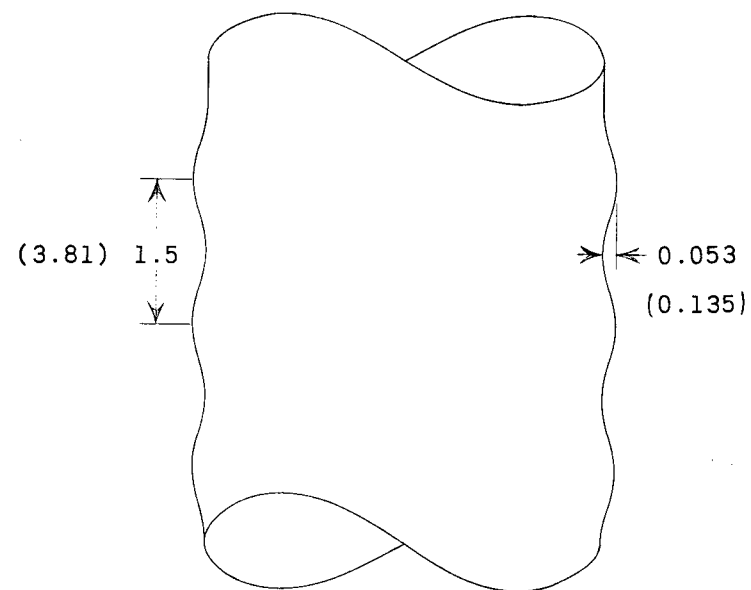
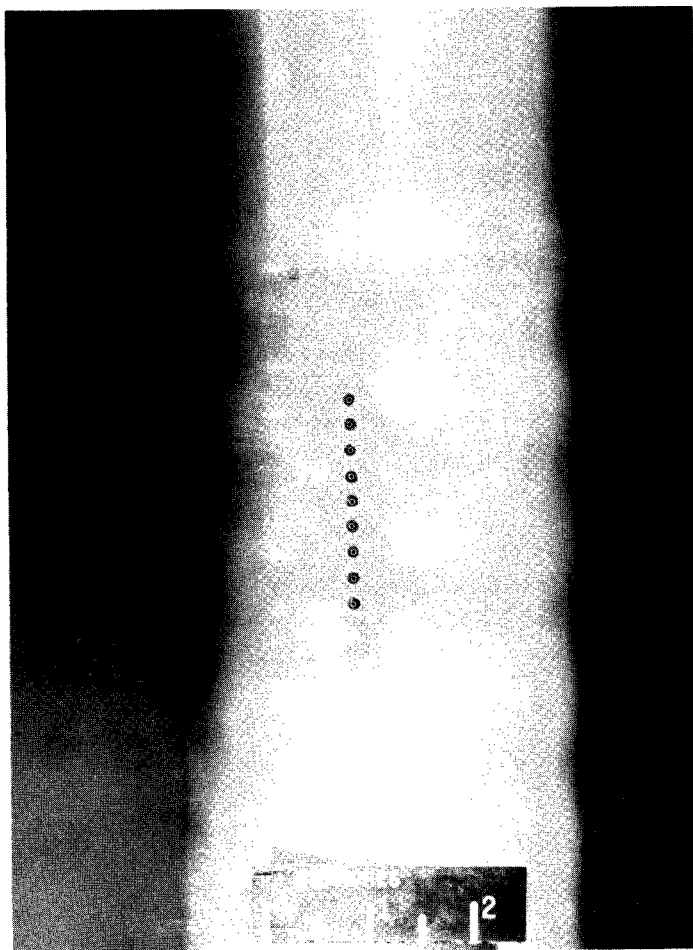


0.053-inch (0.135-cm) transverse creases



(b) 0.017-inch (0.043-cm) and 0.053-inch (0.135-cm) transverse creases.

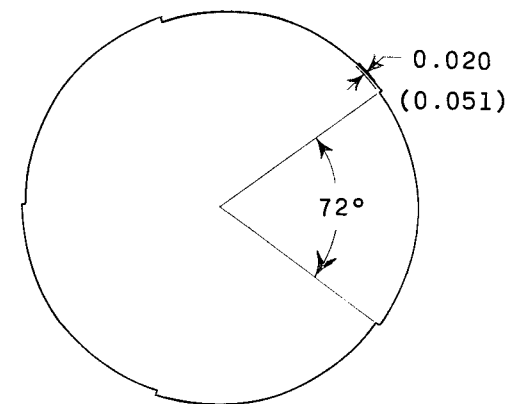
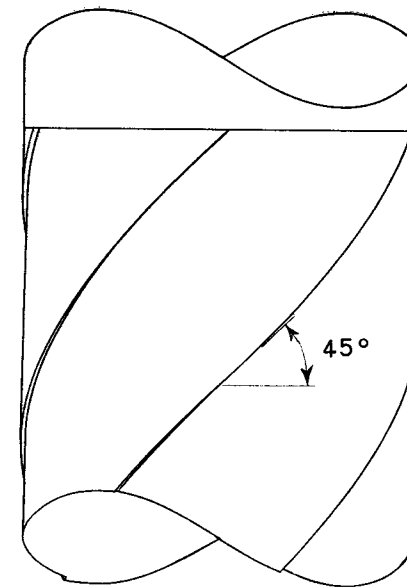
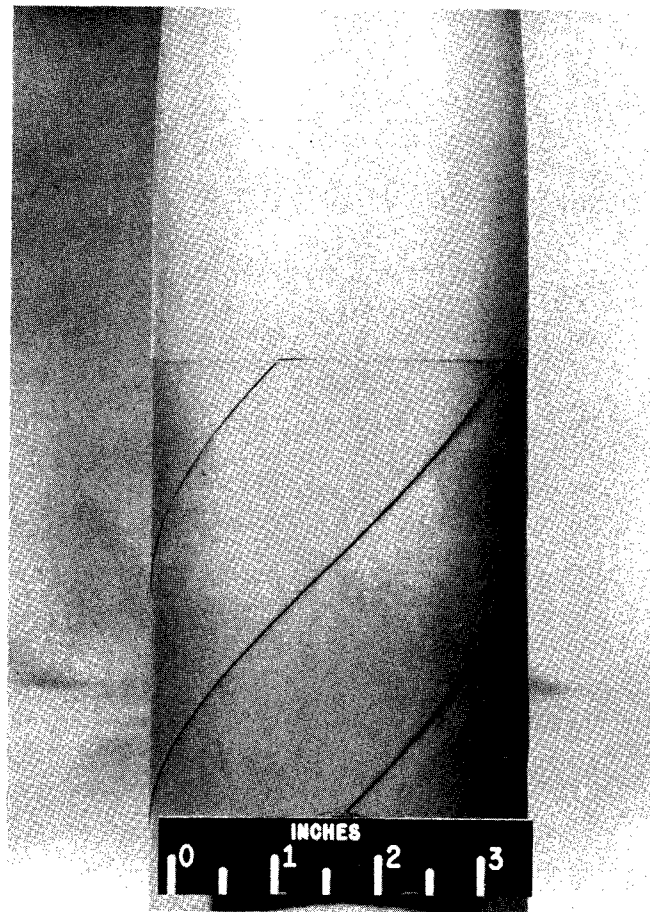
Figure 3.- Continued.



(c) 0.053-inch (0.135-cm) protruding waves.

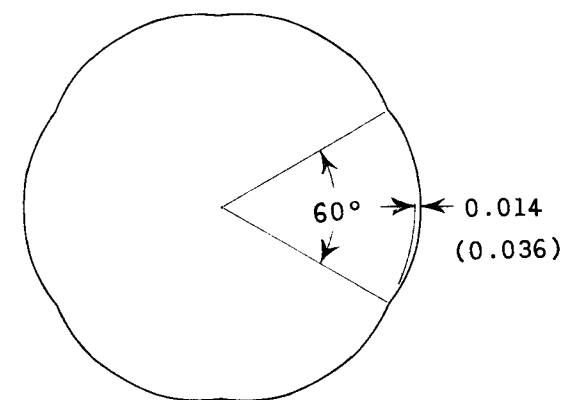
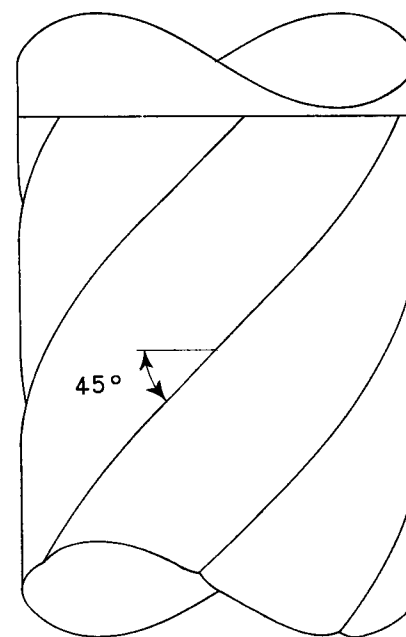
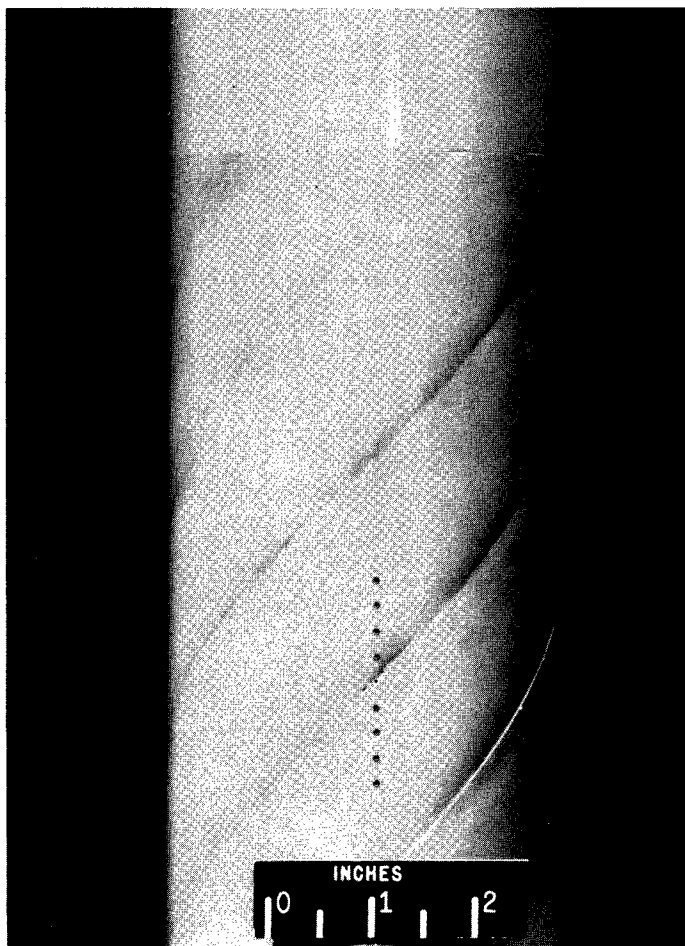
L-61-1043

Figure 3.- Continued.



(d) 0.020-inch (0.051-cm) 45° rearward steps.

Figure 3.- Continued.



(e) 0.014-inch (0.036-cm) 45° creases.

L-61-1046

Figure 3.- Concluded.

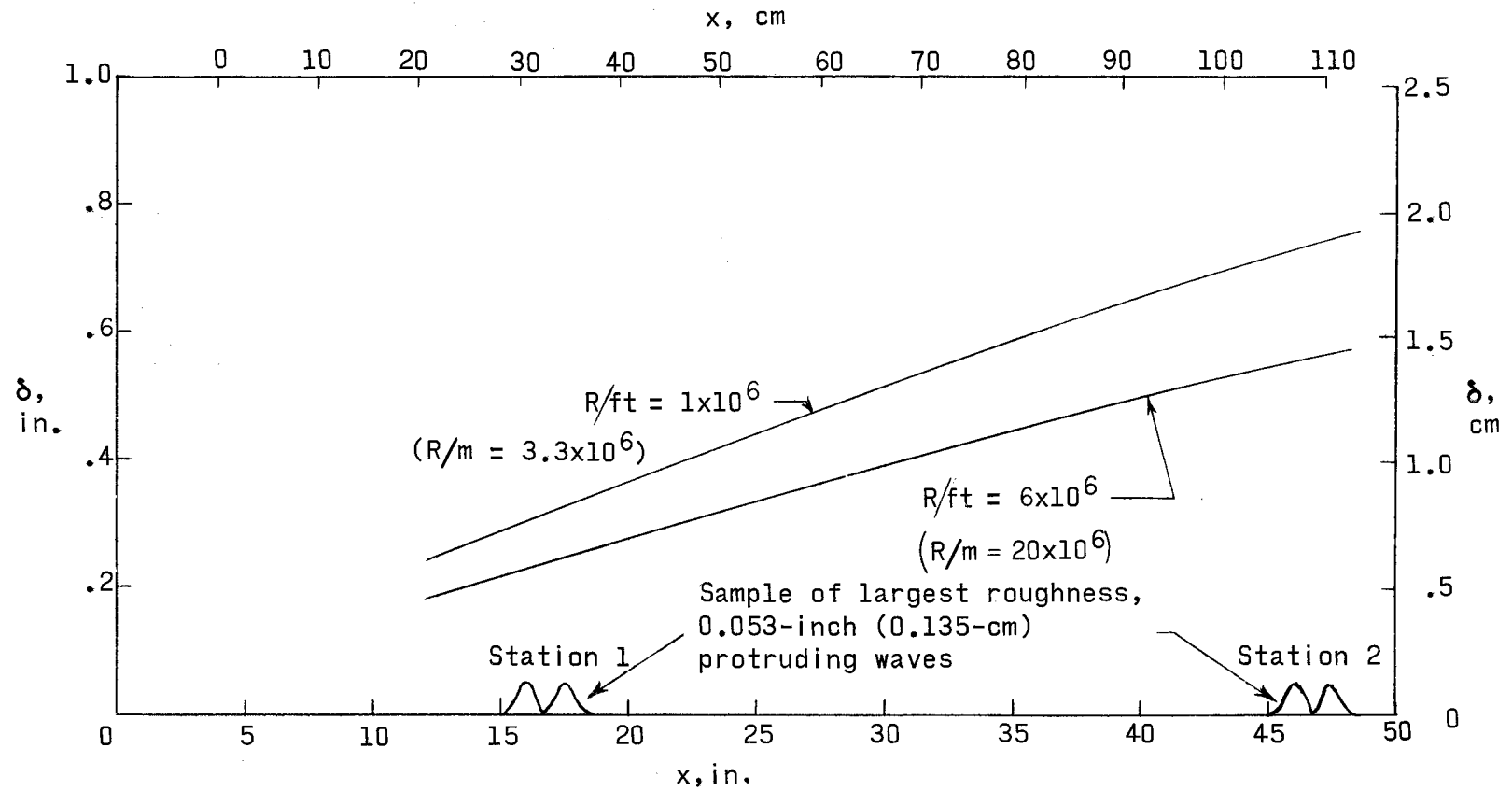


Figure 4.- Comparison of estimated total boundary-layer thickness δ for configuration with highest roughness, 0.053-inch (0.135-cm) protruding waves. $M_\infty = 1.00$.

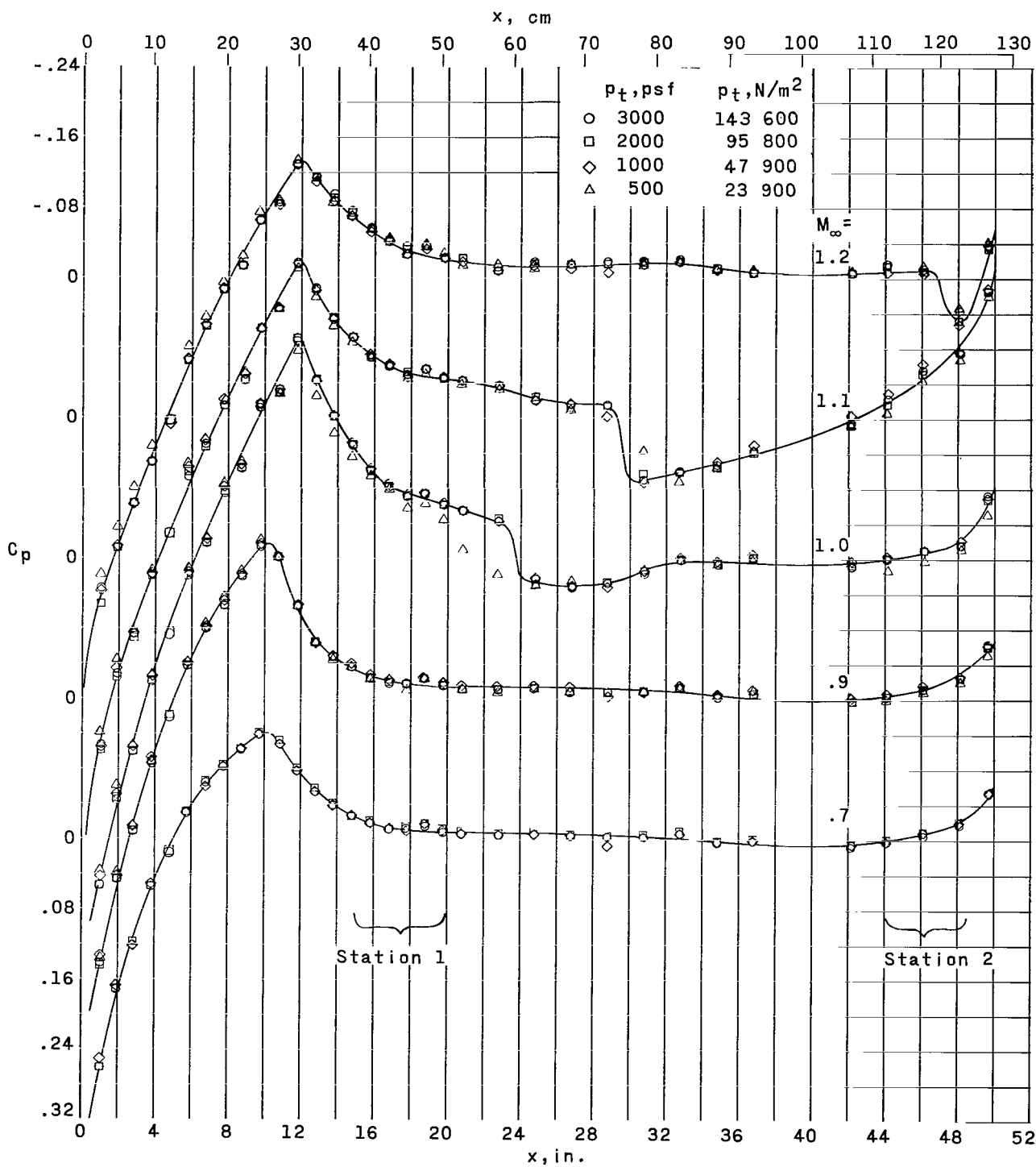
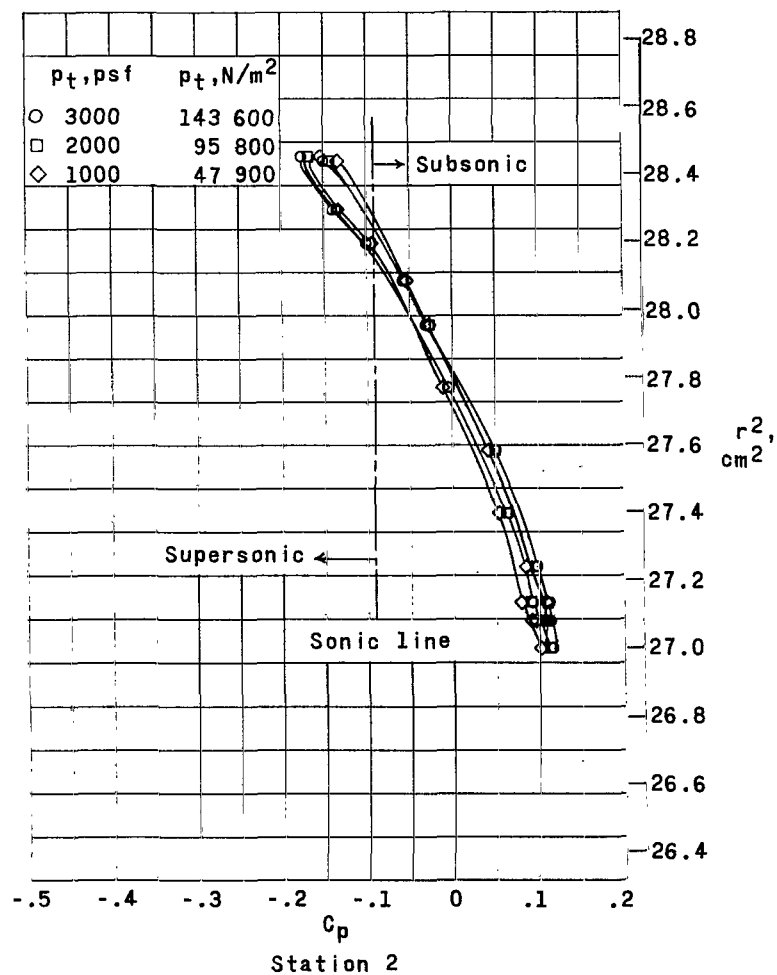
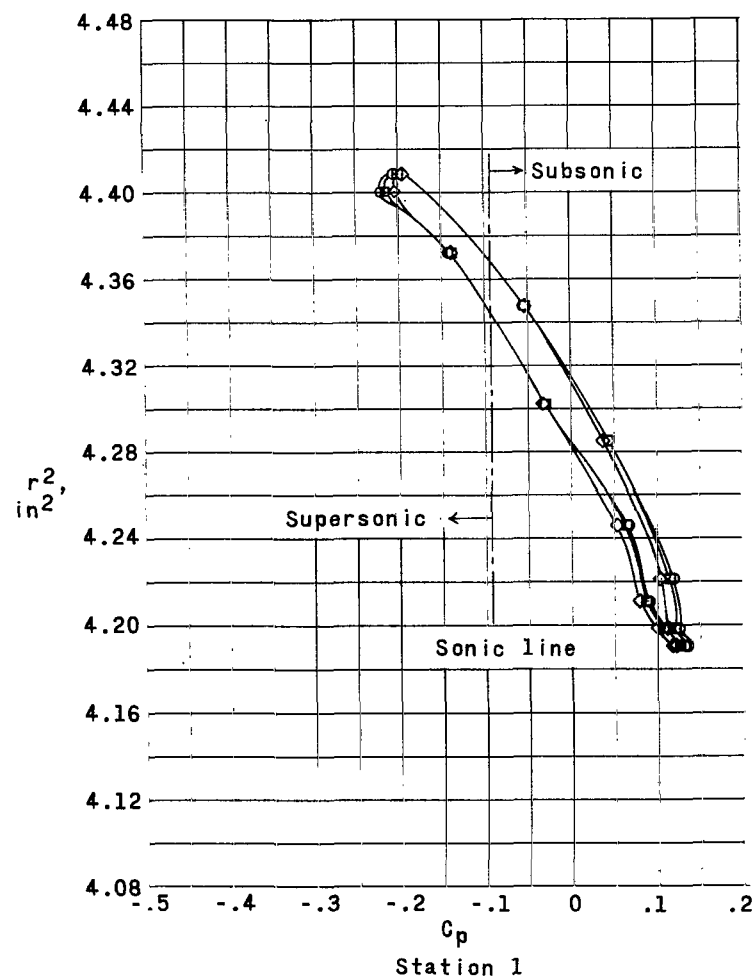
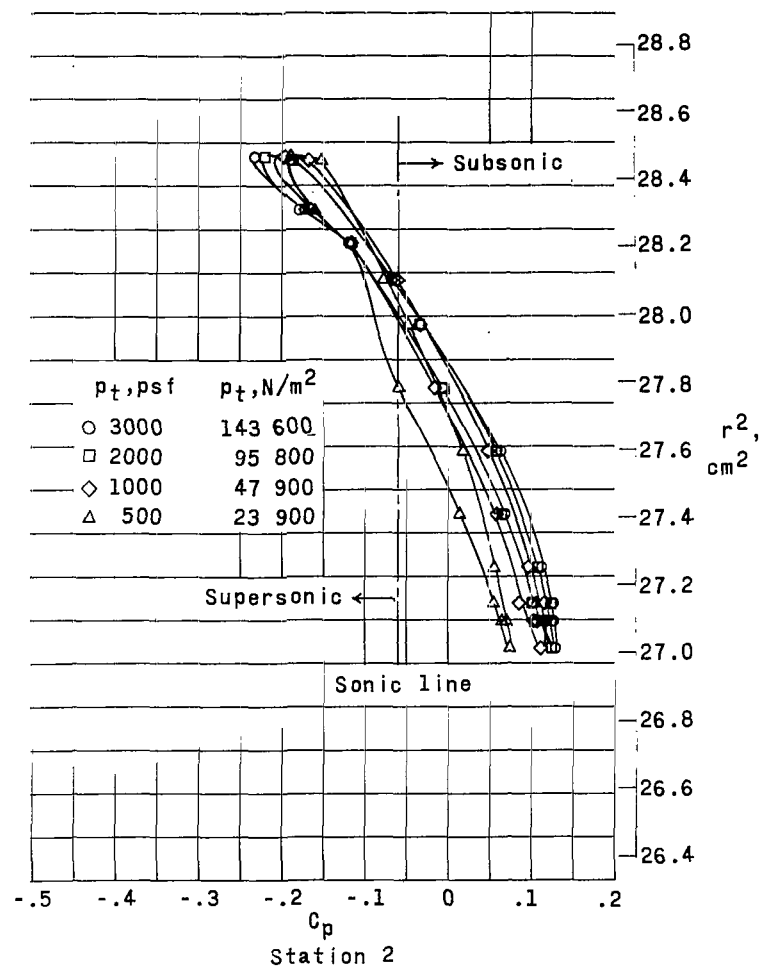
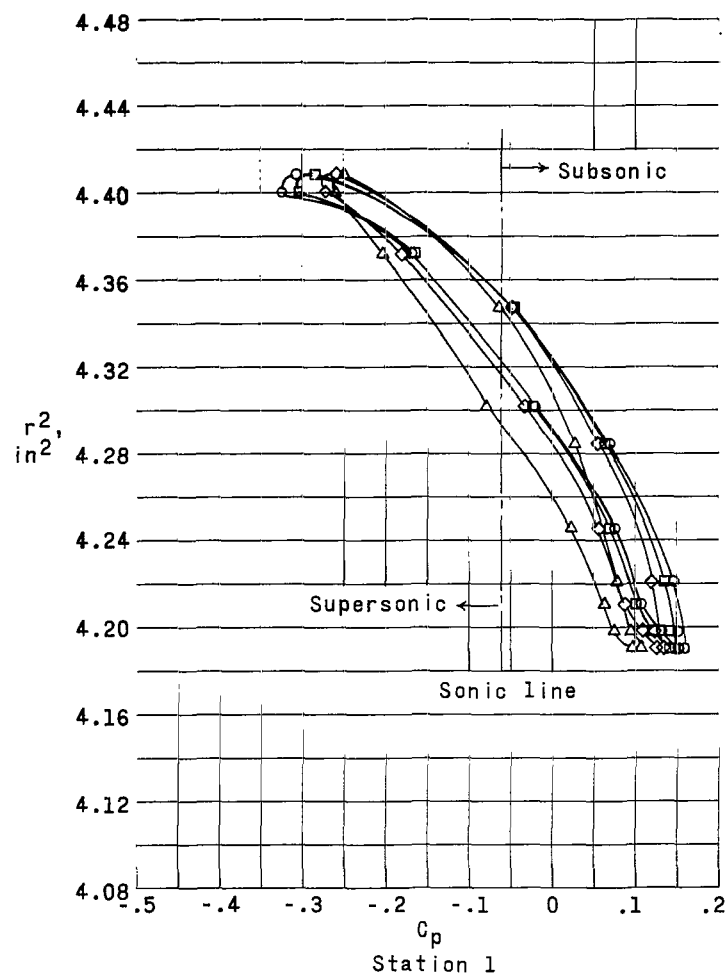


Figure 5.- Pressure distributions over basic smooth model.



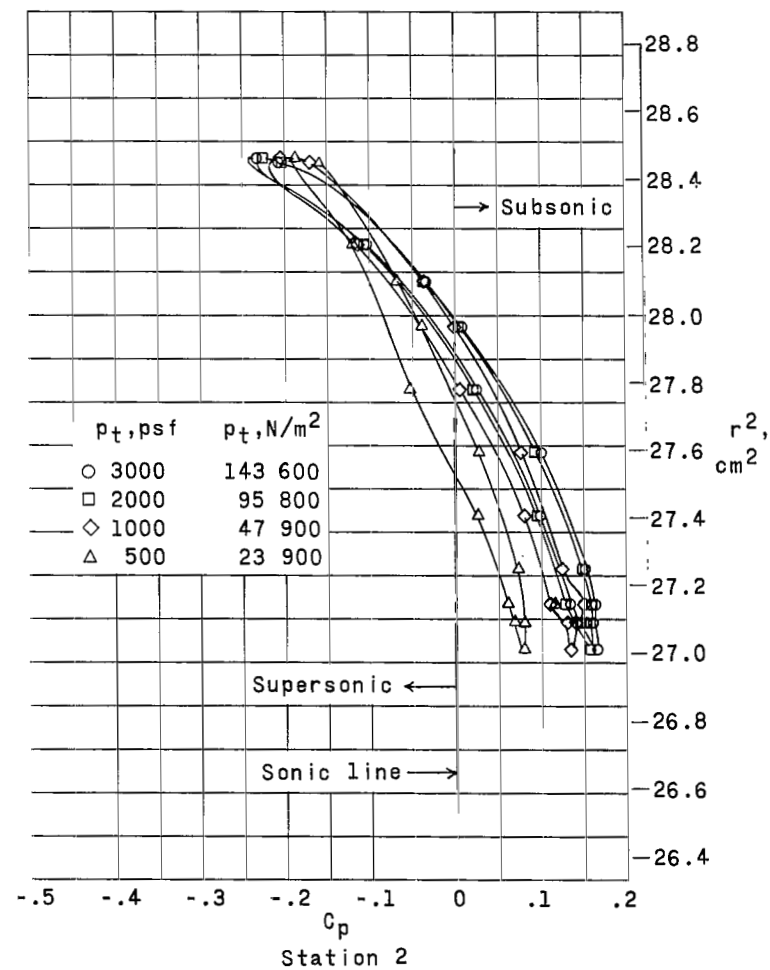
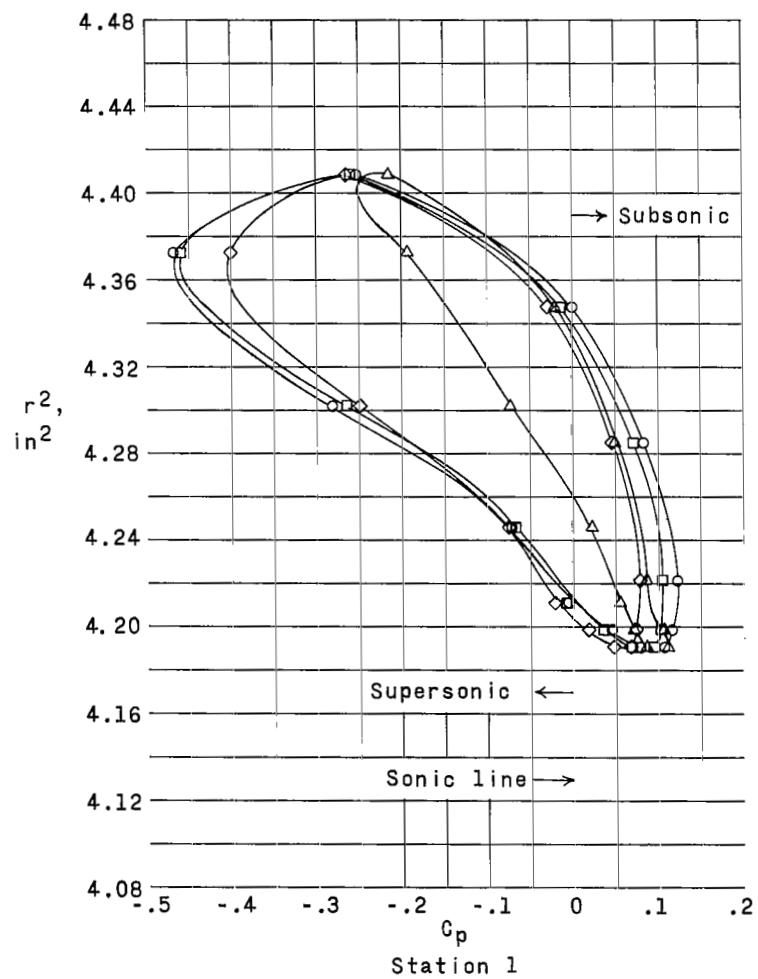
(a) $M_\infty = 0.70$.

Figure 6.- Variation of C_p with r^2 . Model with 0.053-inch (0.135-cm) protruding waves.



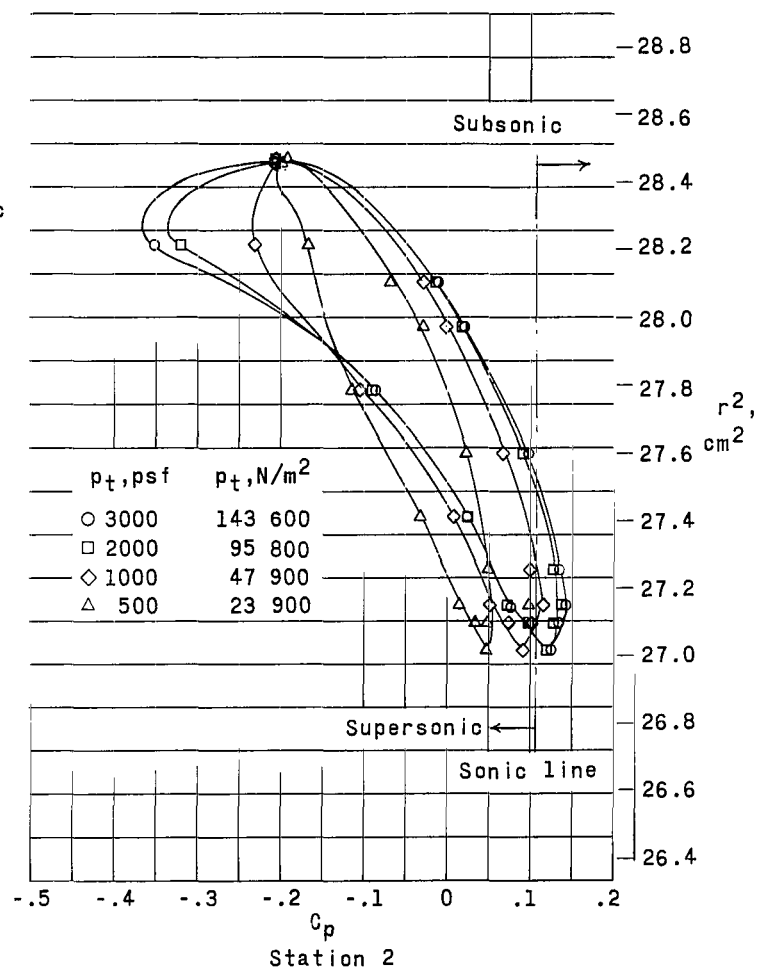
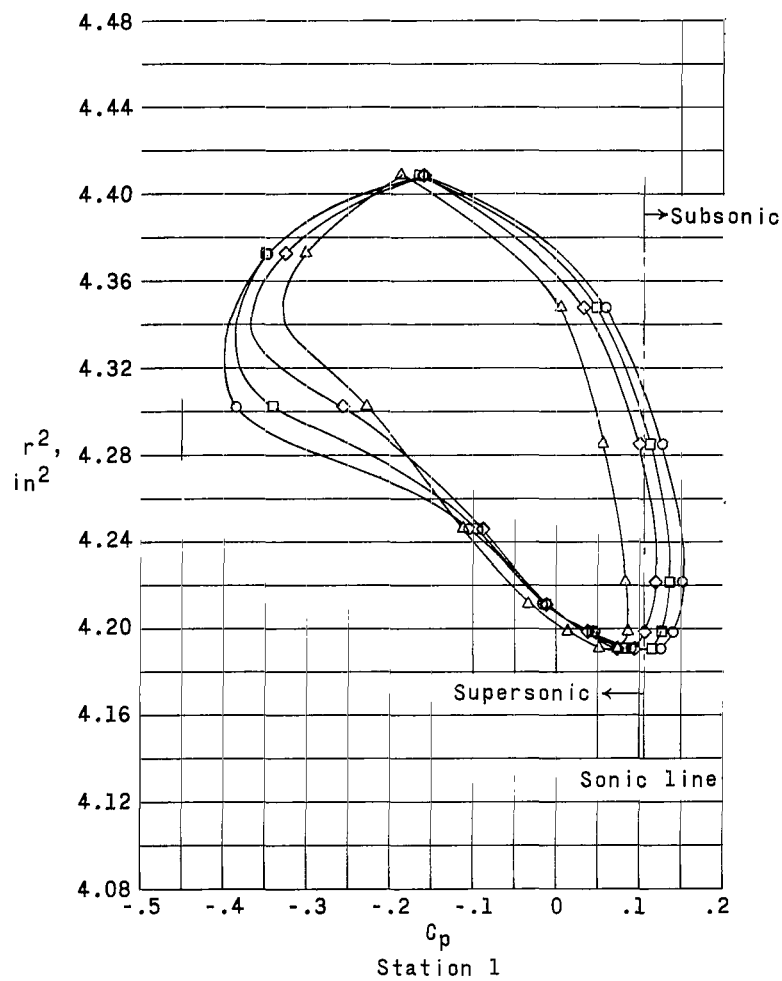
(b) $M_\infty = 0.90$.

Figure 6.- Continued.

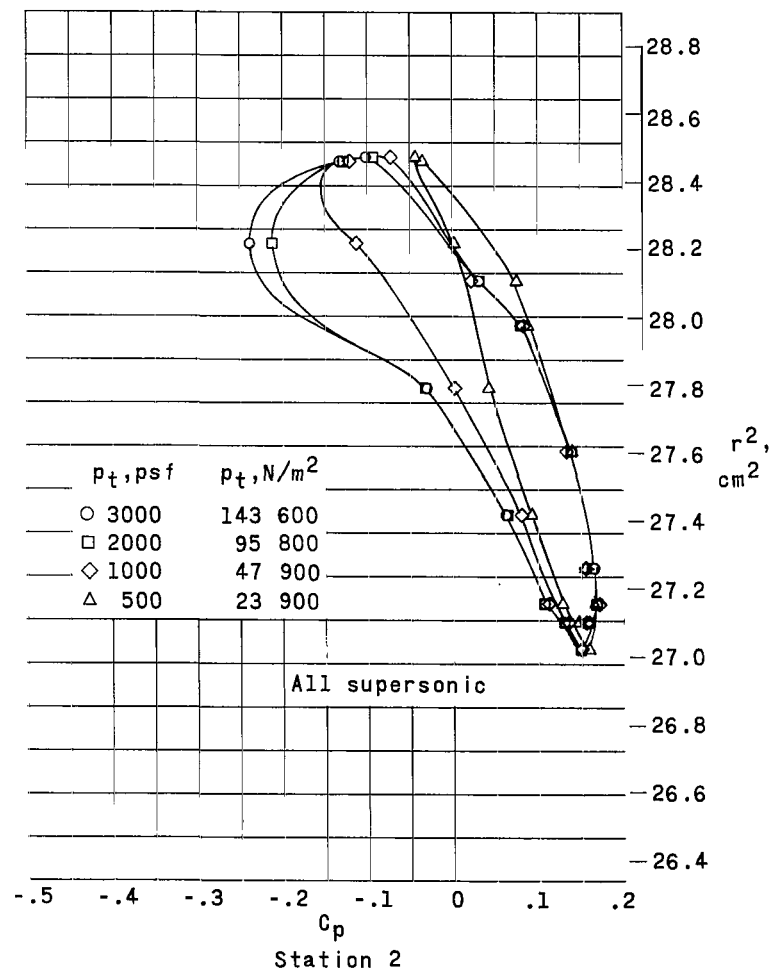
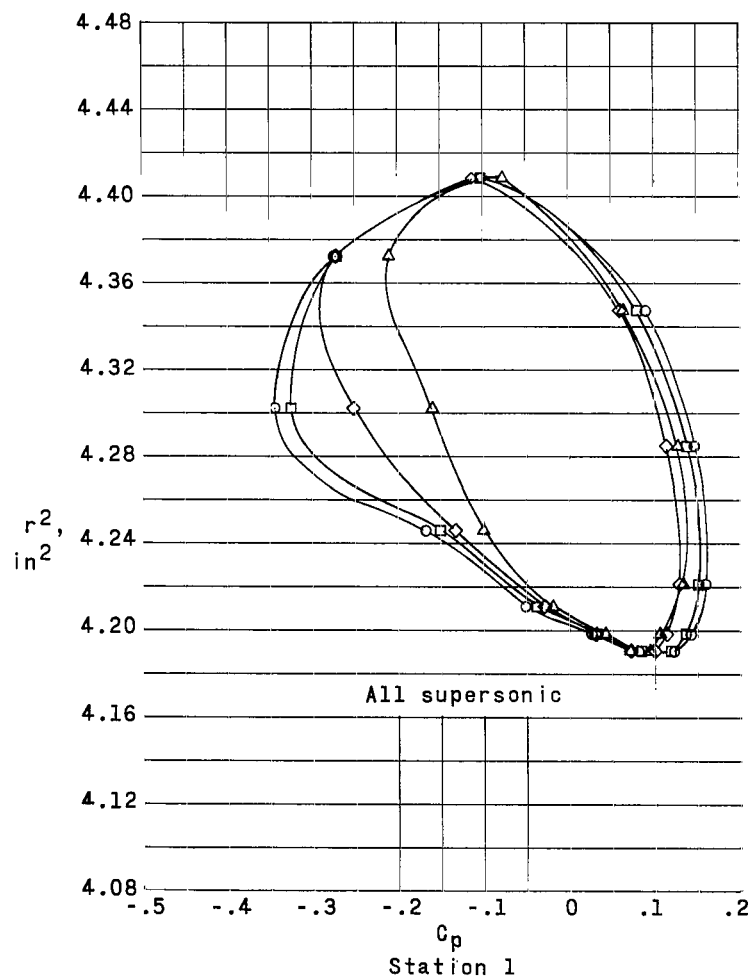


(c) $M_\infty = 1.00$.

Figure 6.- Continued.

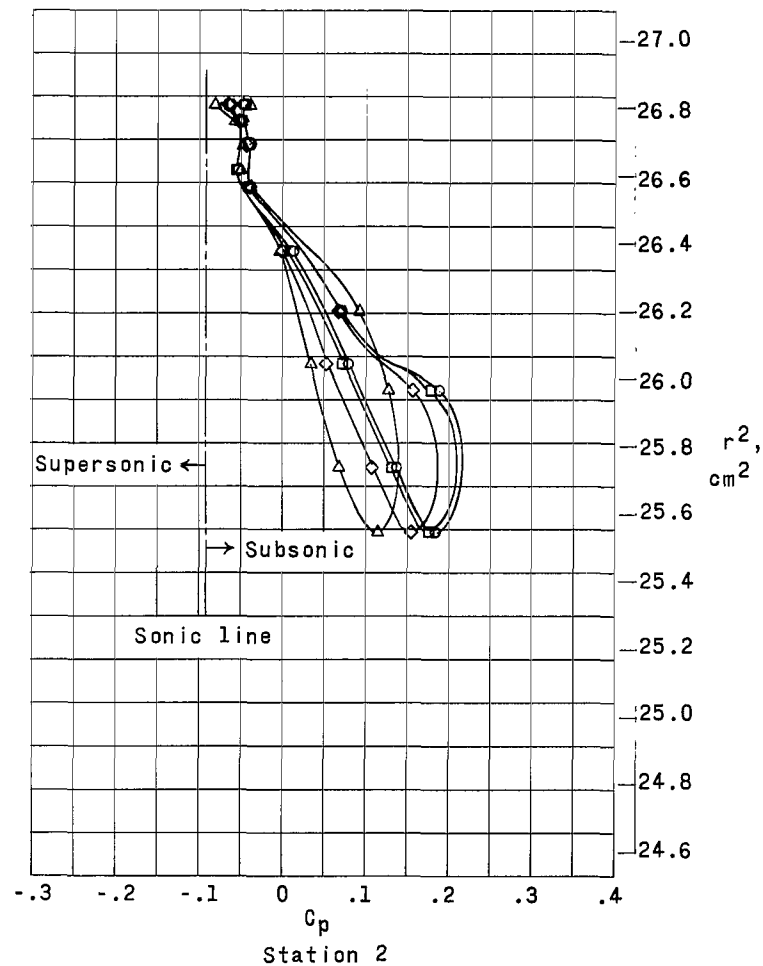
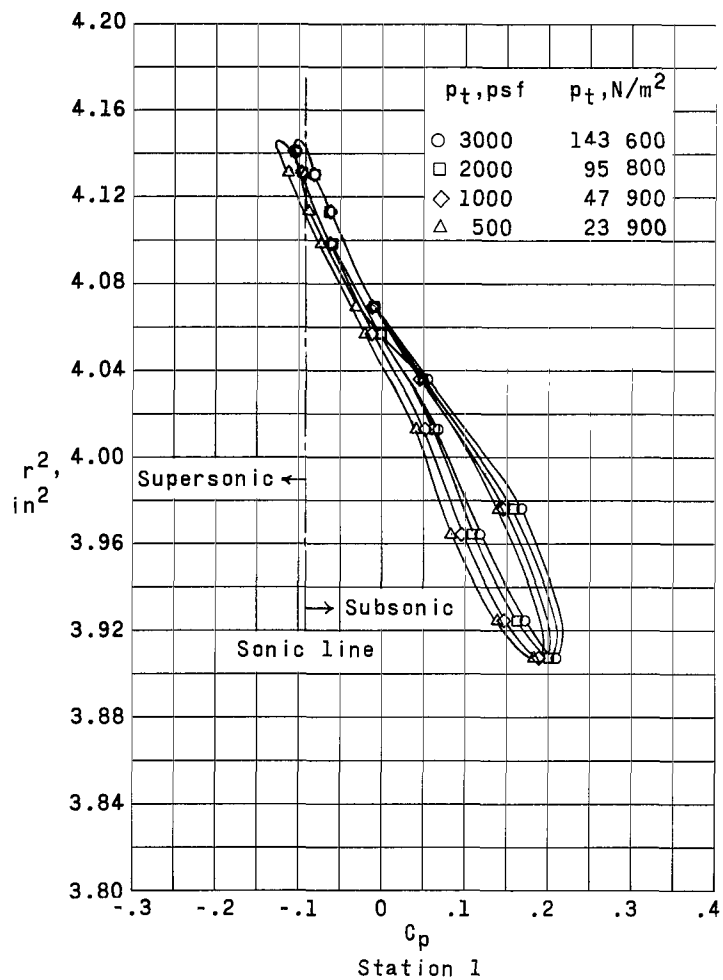


(d) $M_\infty = 1.10$.
Figure 6.- Continued.



(e) $M_\infty = 1.20$.

Figure 6.- Concluded.



(a) $M_\infty = 0.70$.

Figure 7.- Variation of C_p with r^2 . Model with 0.053-inch (0.135-cm) transverse creases.

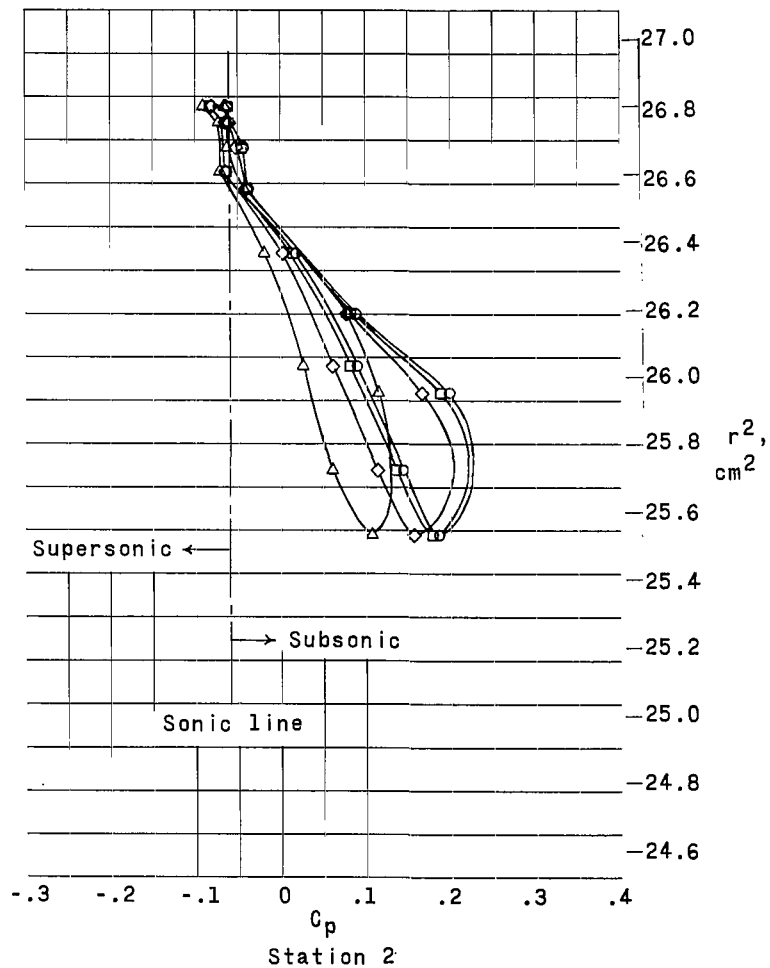
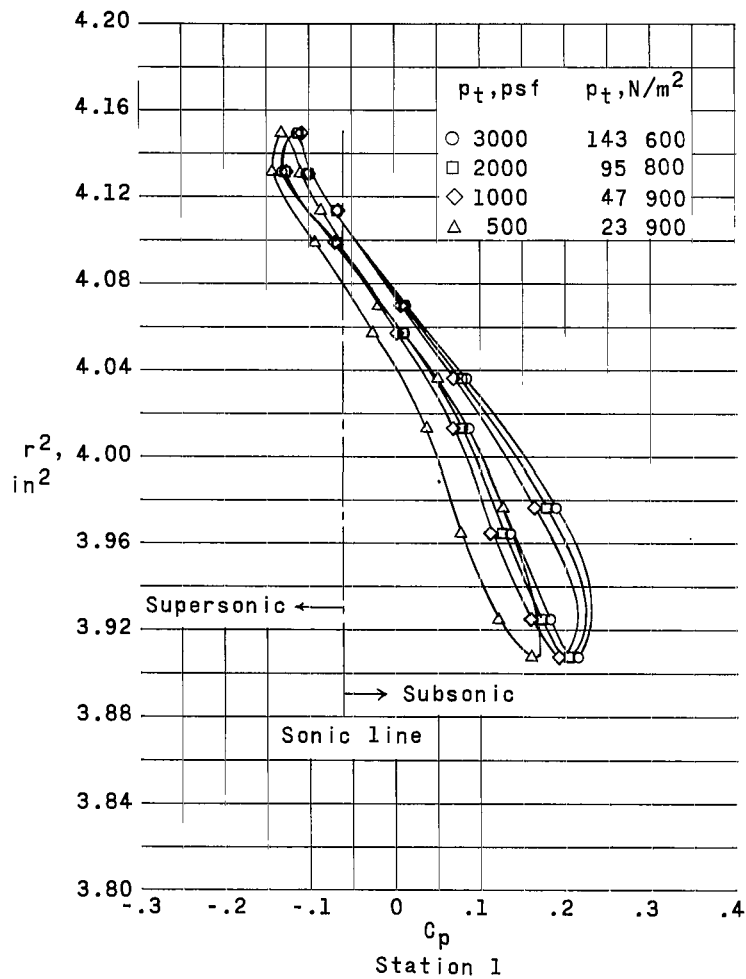
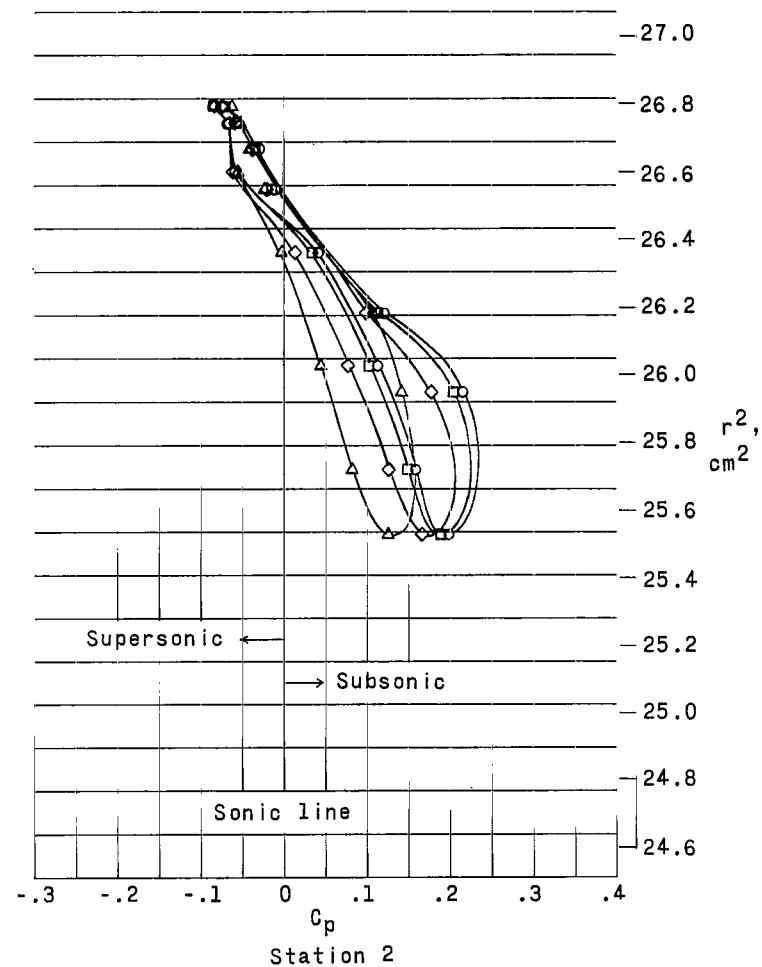
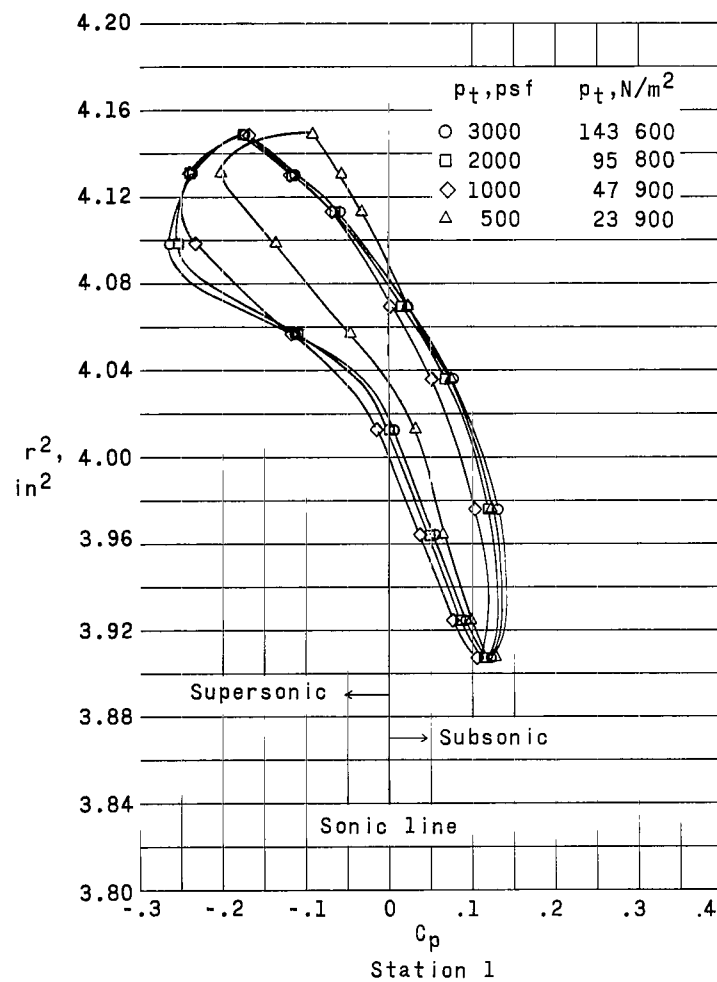
(b) $M_\infty = 0.90$.

Figure 7.- Continued.



(c) $M_\infty = 1.00$.

Figure 7.- Continued.

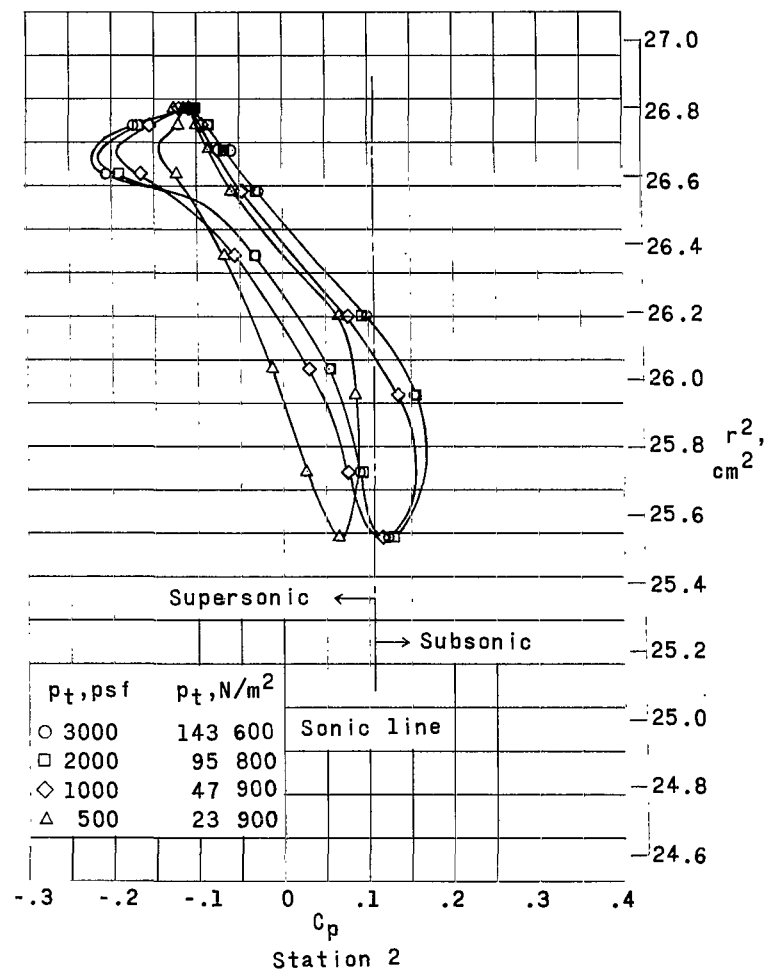
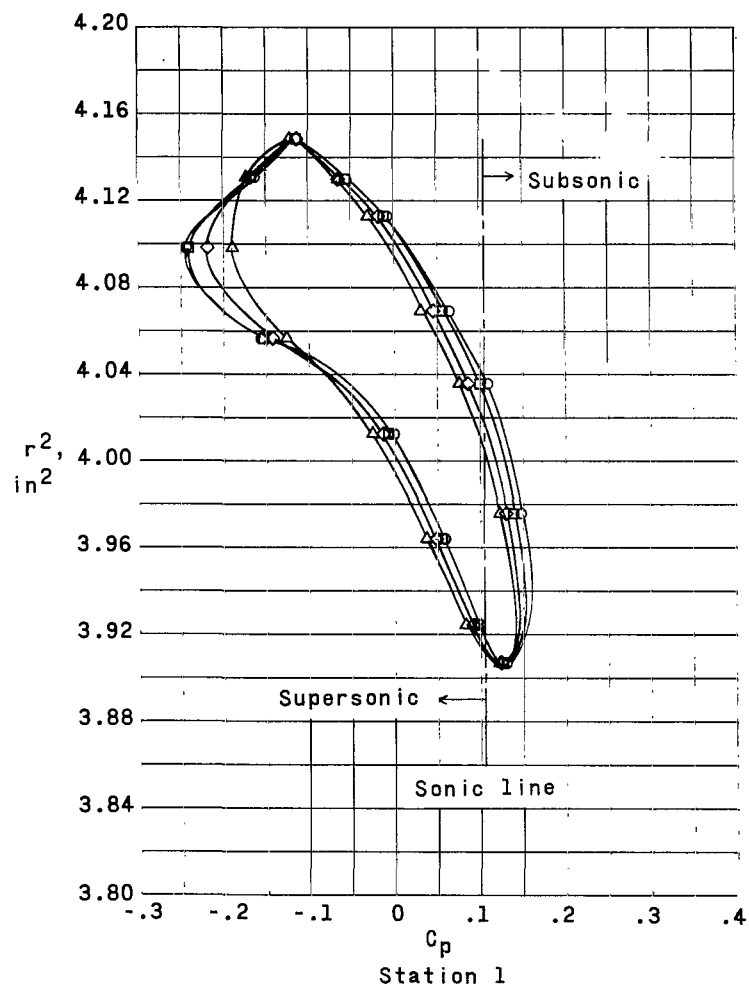
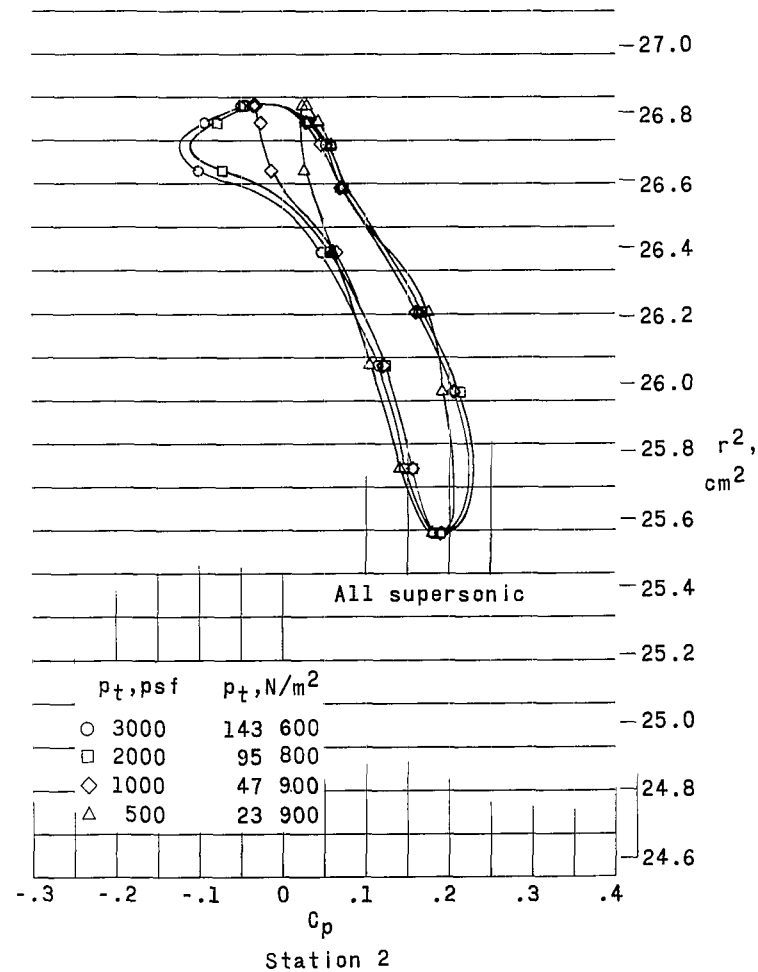
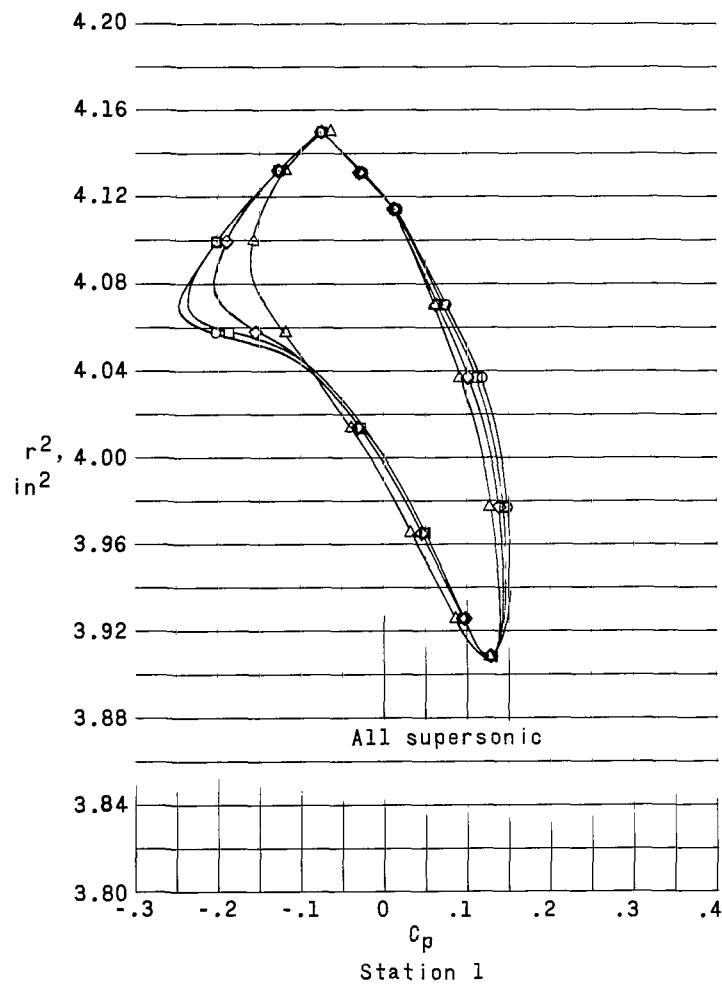
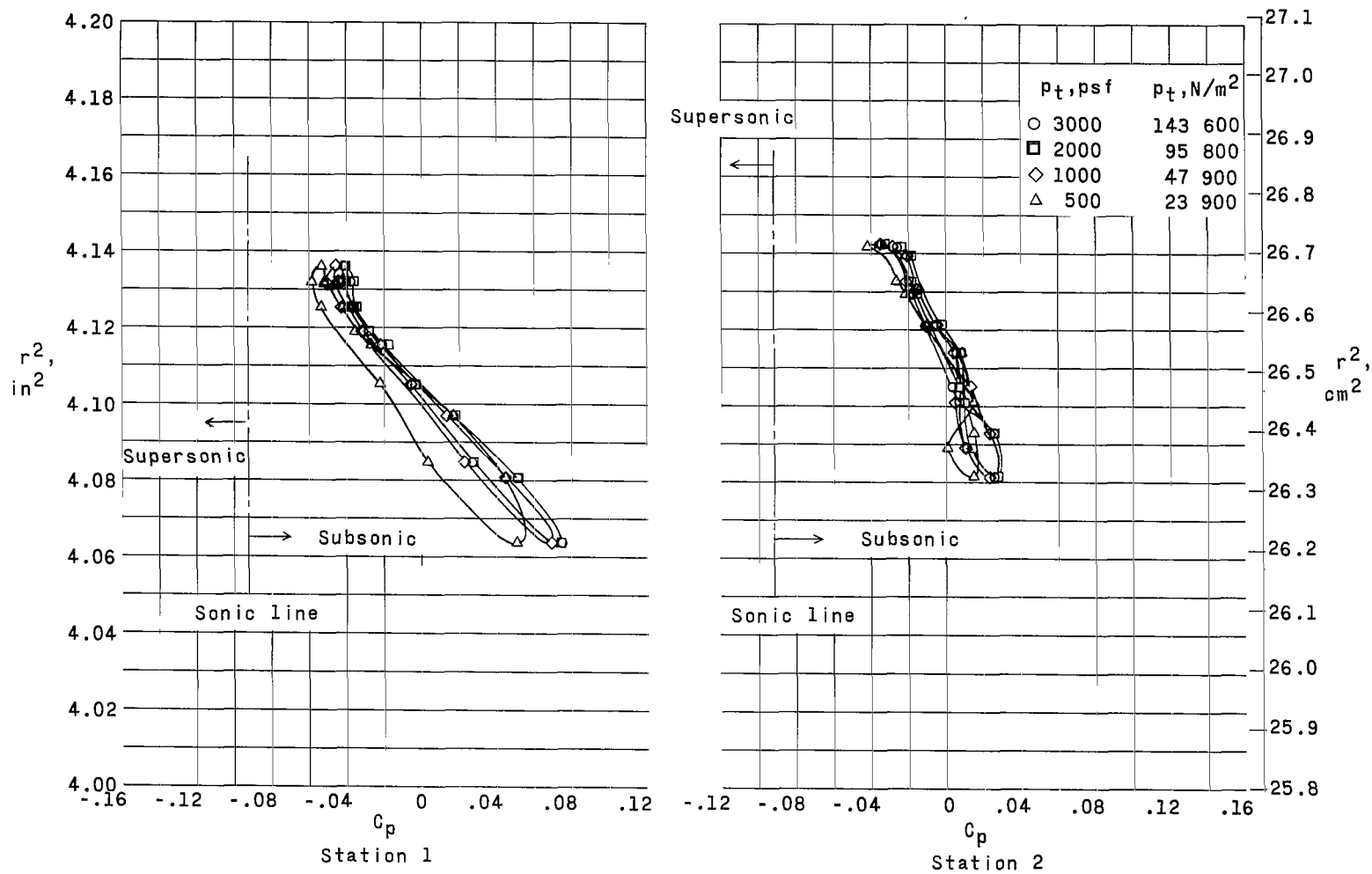
(d) $M_\infty = 1.10$.

Figure 7.- Continued.



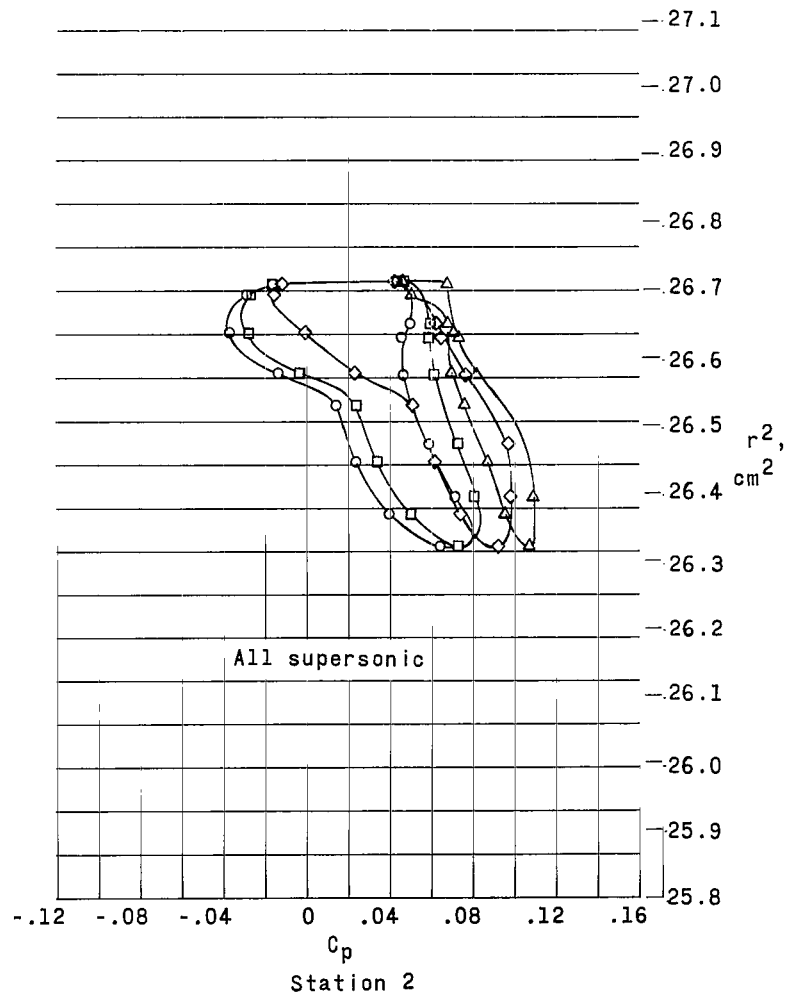
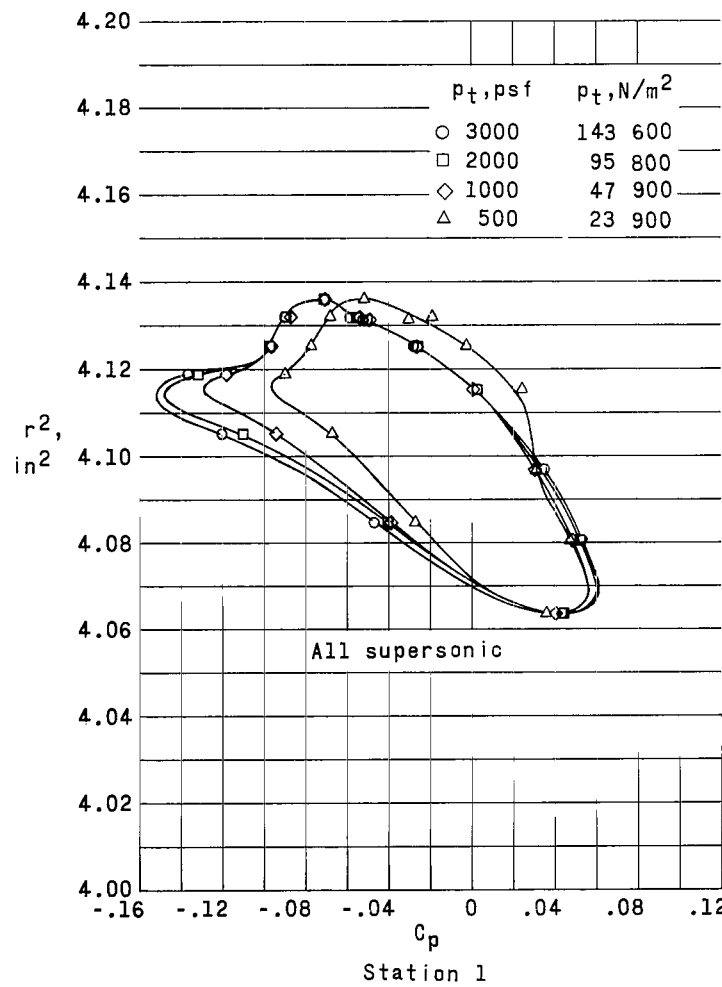
(e) $M_\infty = 1.20$.

Figure 7.- Concluded.



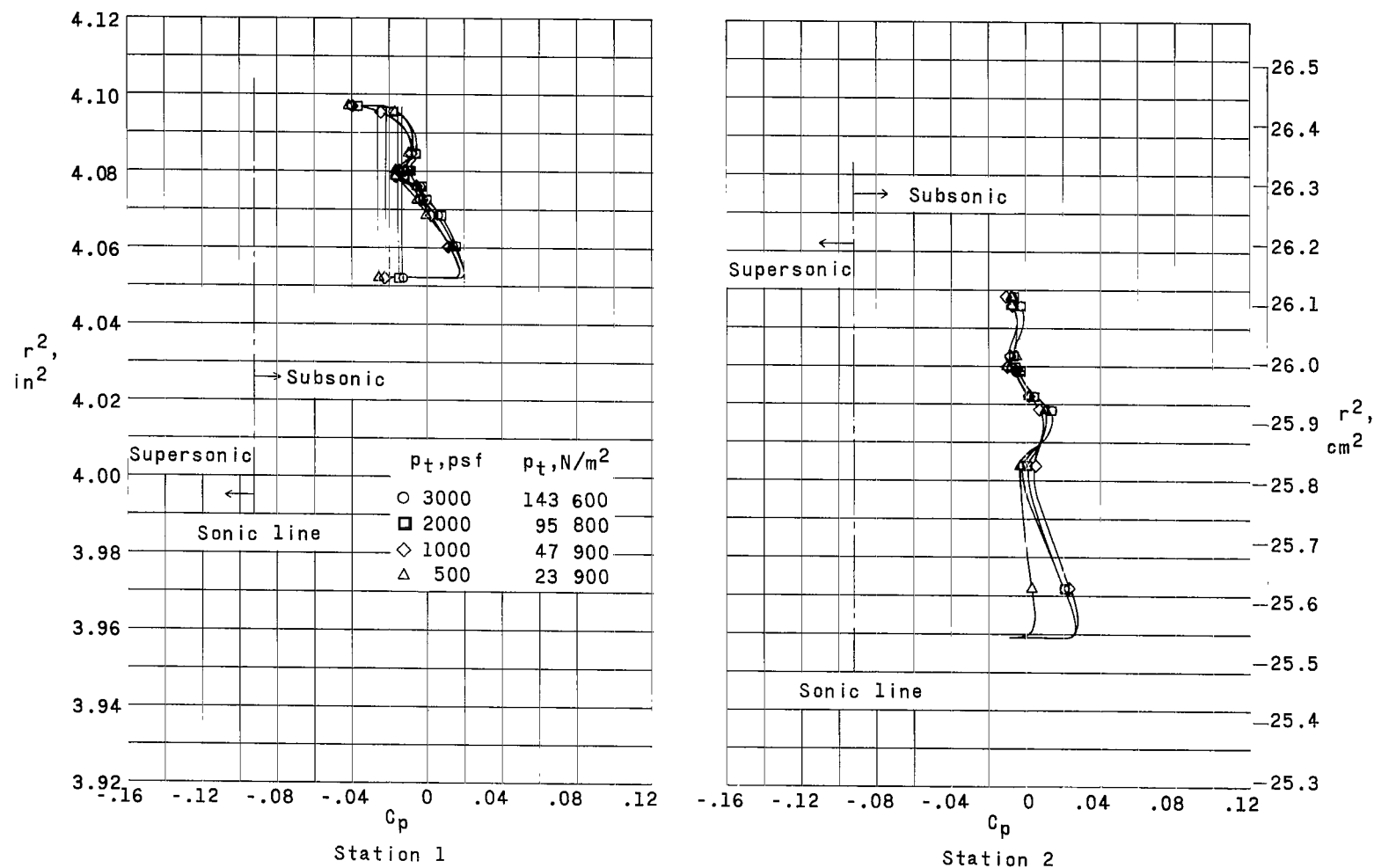
(a) $M_\infty = 0.70$.

Figure 8.- Variation of C_p with r^2 . Model with 0.017-inch (0.043-cm) transverse creases.



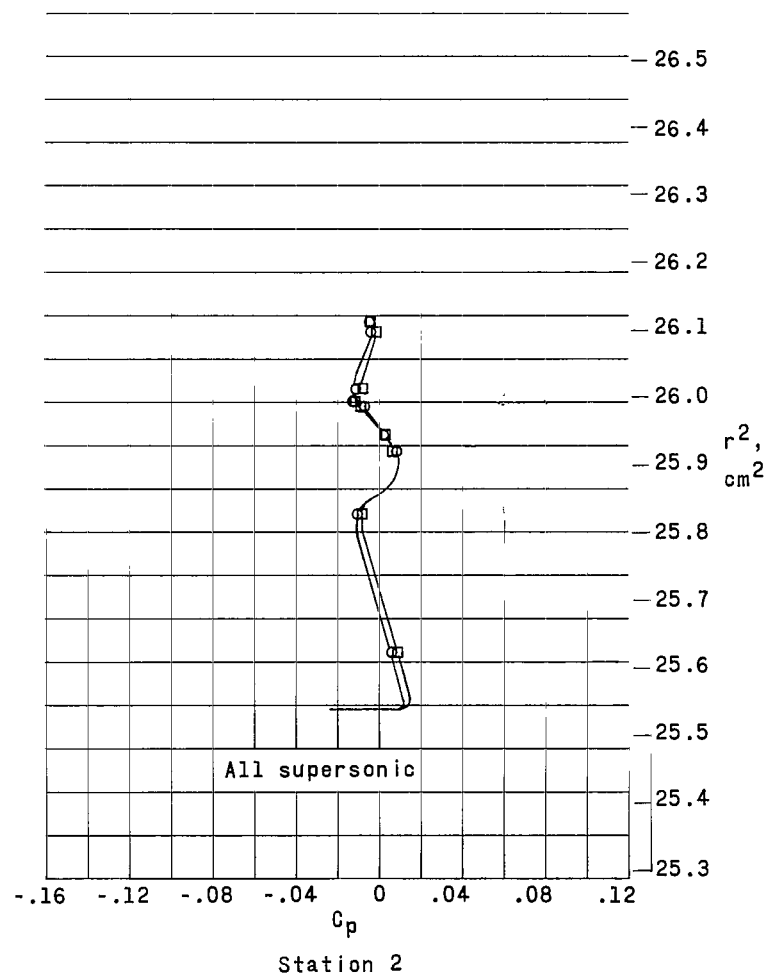
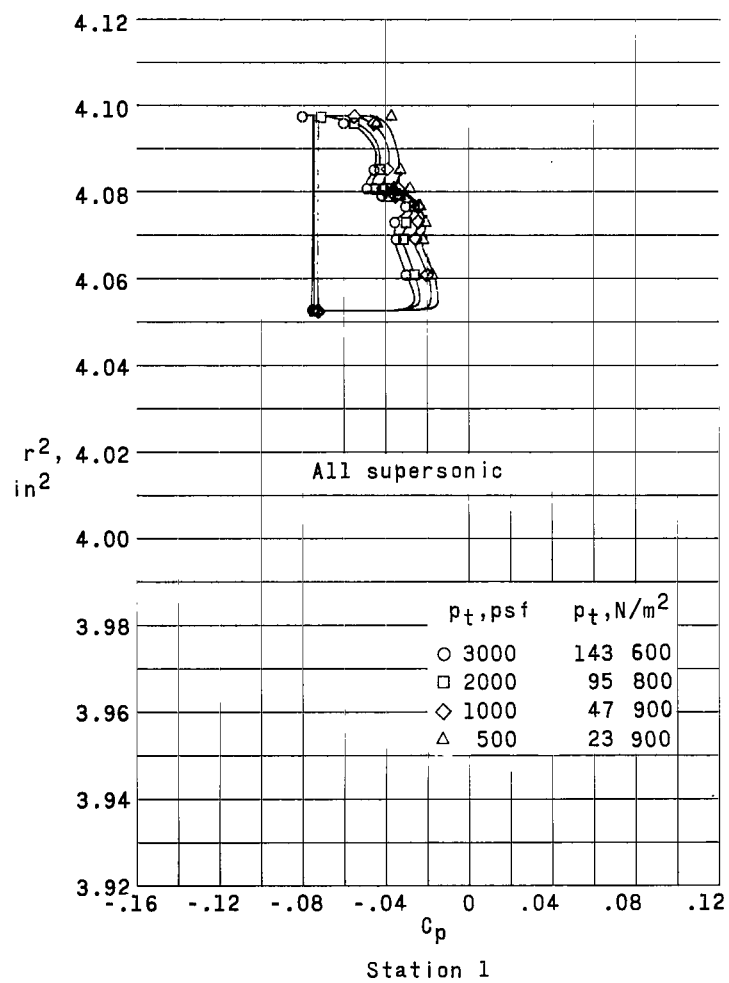
(b) $M_\infty = 1.20$.

Figure 8.- Concluded.



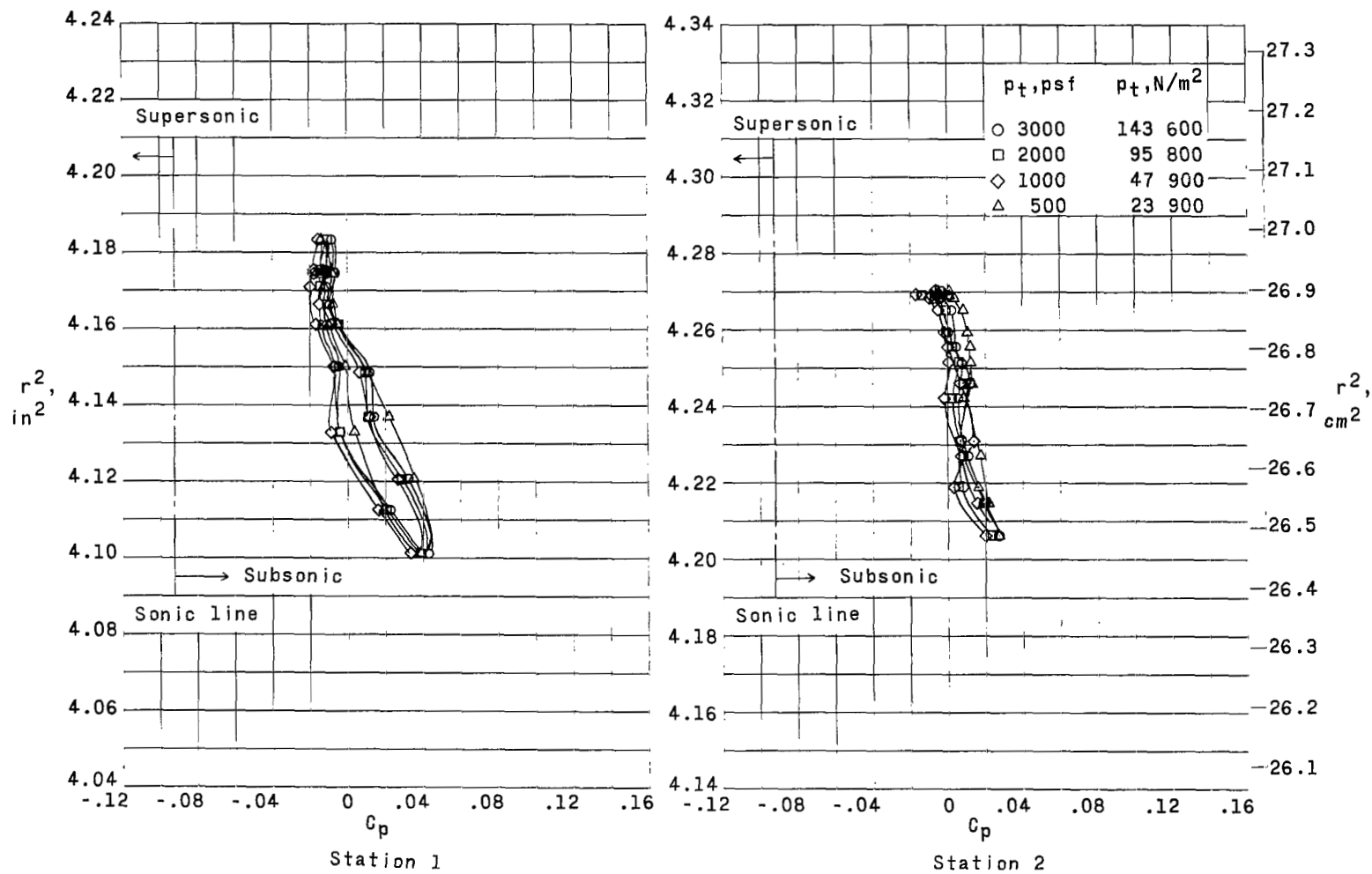
(a) $M_\infty = 0.70$.

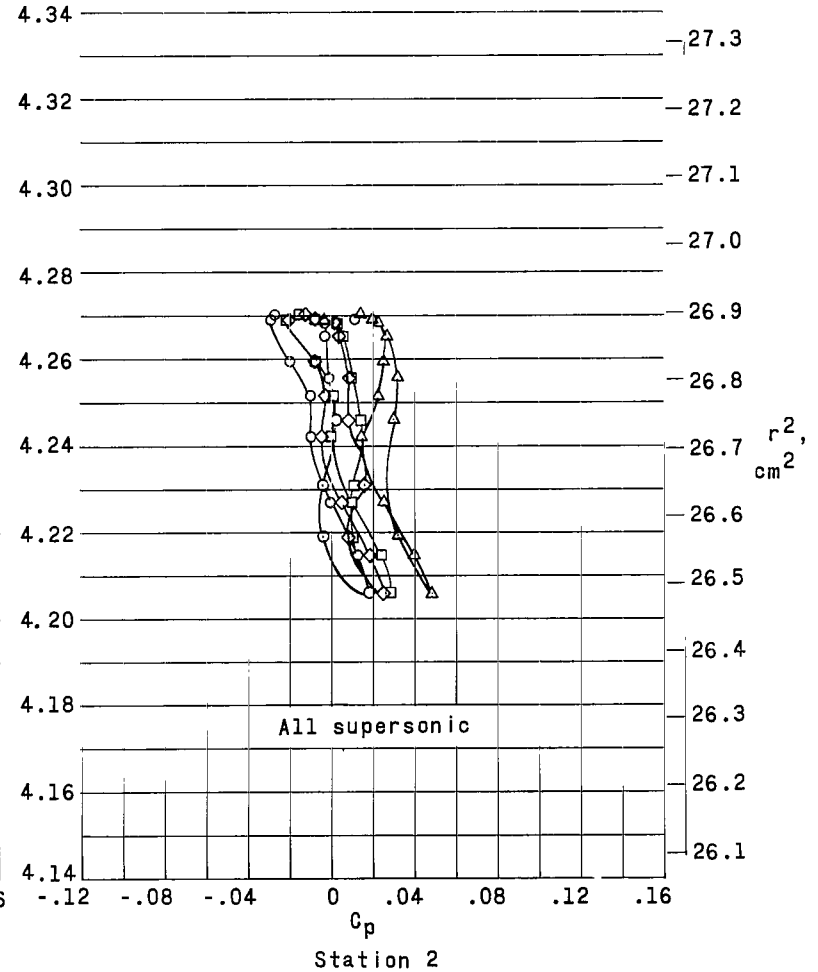
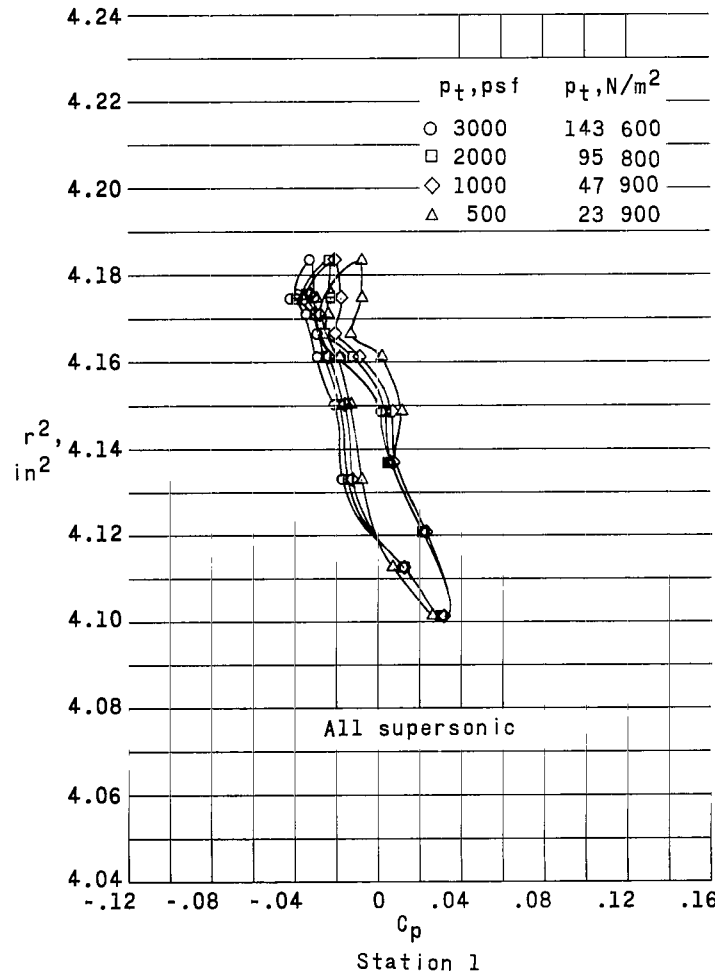
Figure 9.- Variation of C_p with r^2 . Model with 0.020-inch (0.051-cm) 45° rearward steps.



(b) $M_\infty = 1.20$.

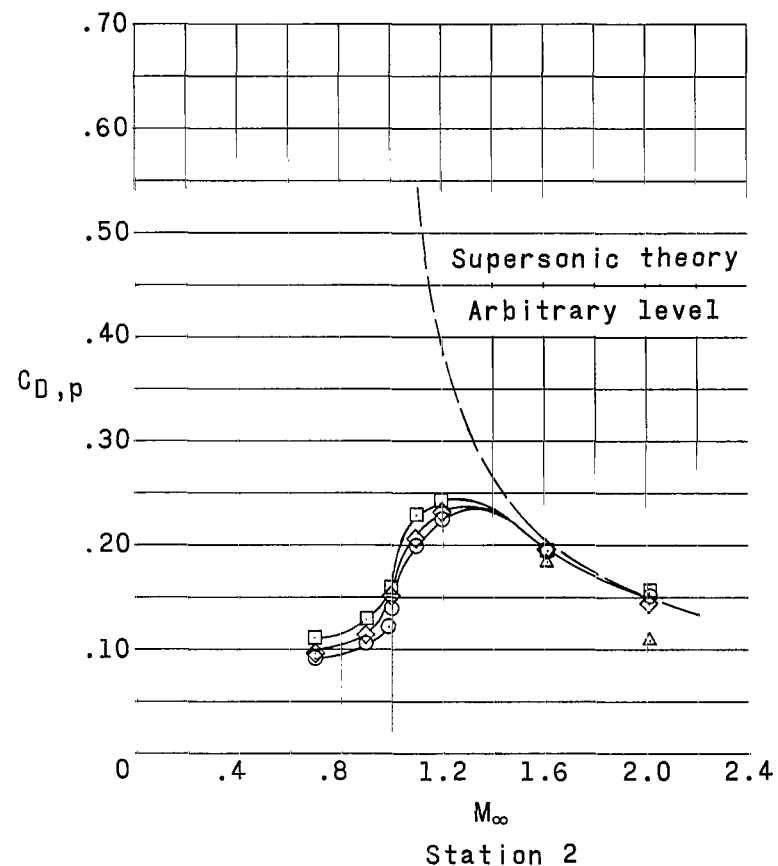
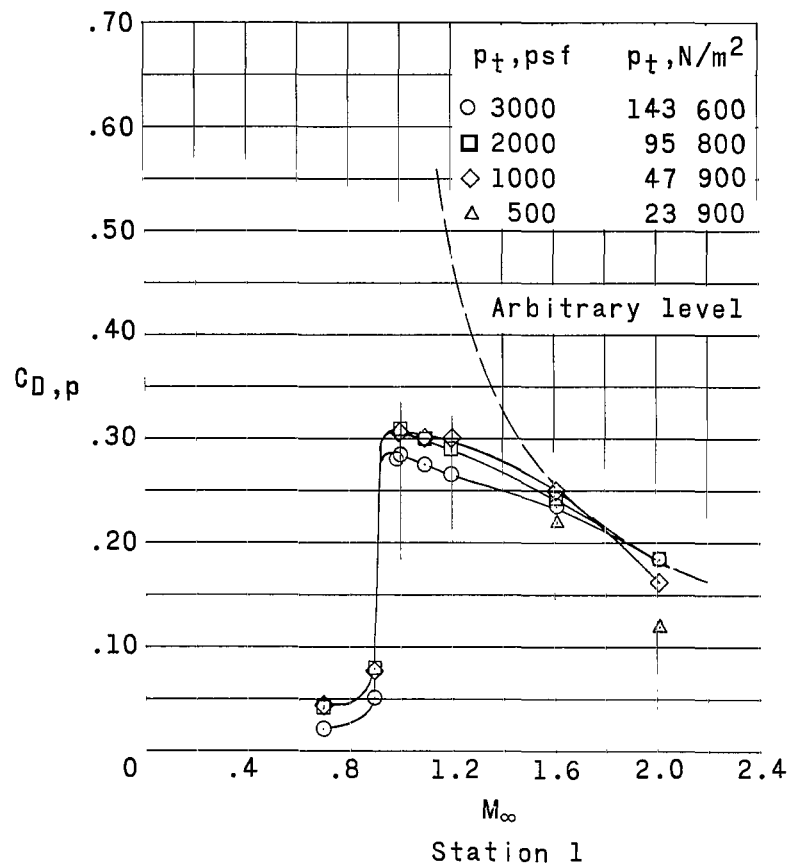
Figure 9.- Concluded.

(a) $M_\infty = 0.70$.Figure 10.- Variation of C_p with r^2 . Model with 0.014-inch (0.036-cm) 45° creases.



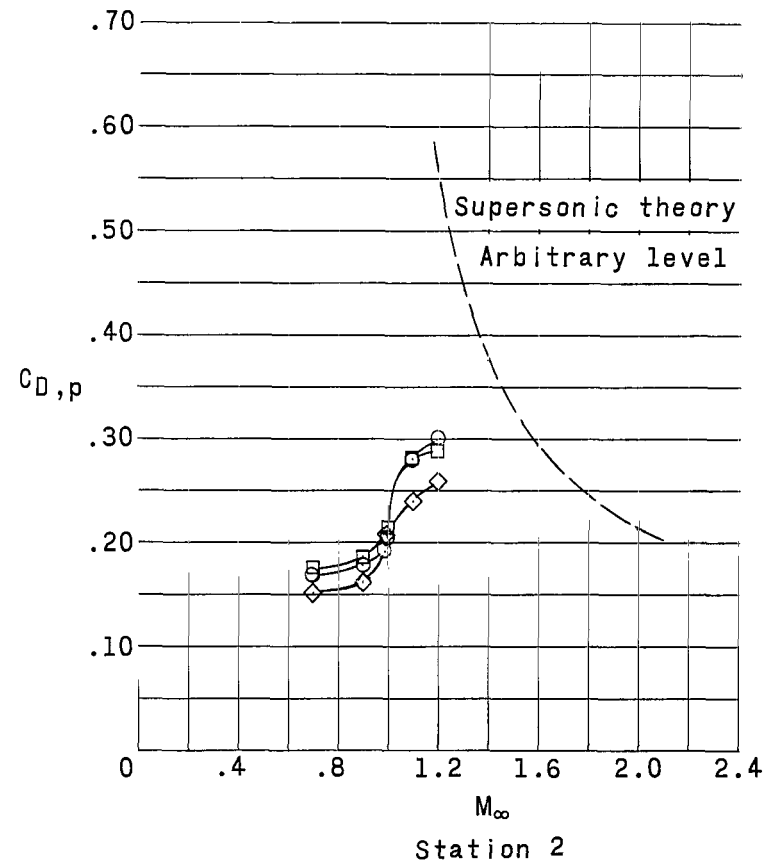
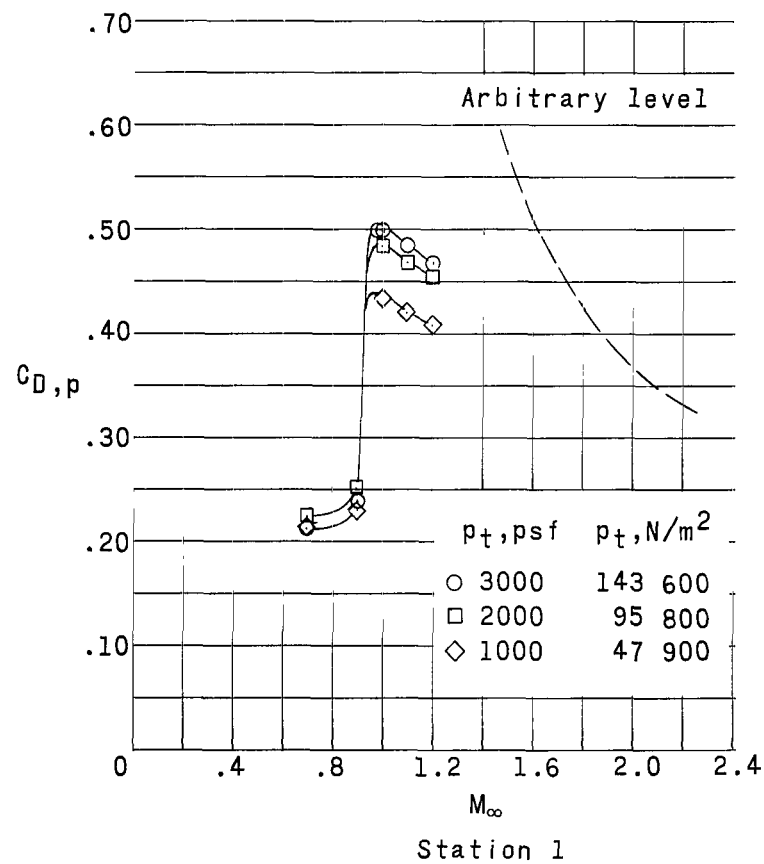
(b) $M_\infty = 1.20$.

Figure 10.- Concluded.



(a) Based on original orifices closest to step faces.

Figure 11.- Variation of pressure-drag coefficient $C_{D,p}$ with M_{∞} . Model with 0.021-inch (0.053-cm) steps with grooves.



(b) Based on new orifices closest to step faces.

Figure 11.- Concluded.

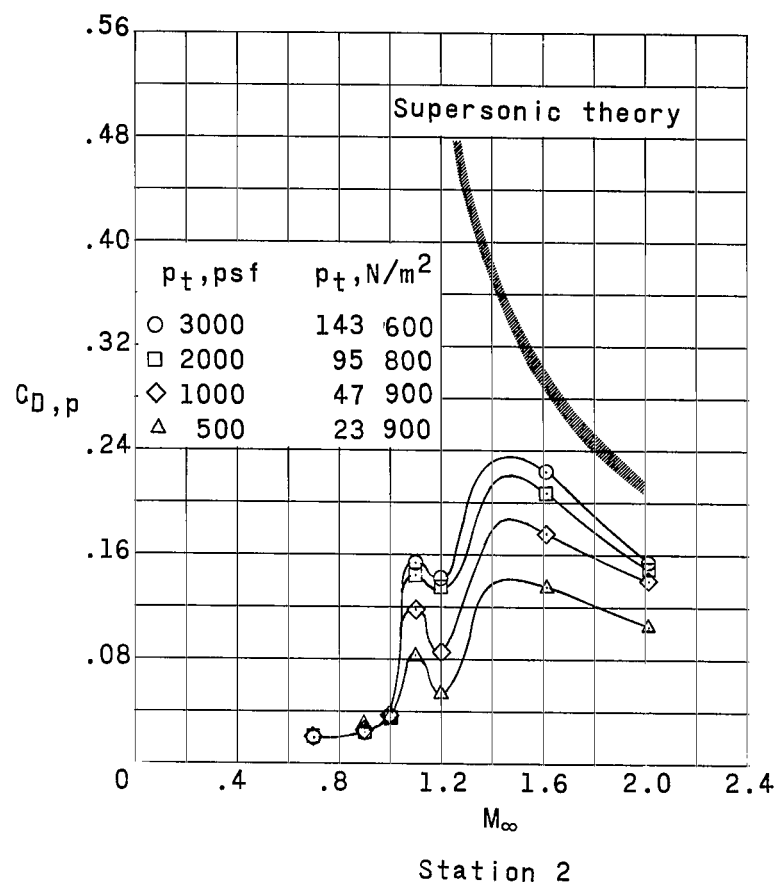
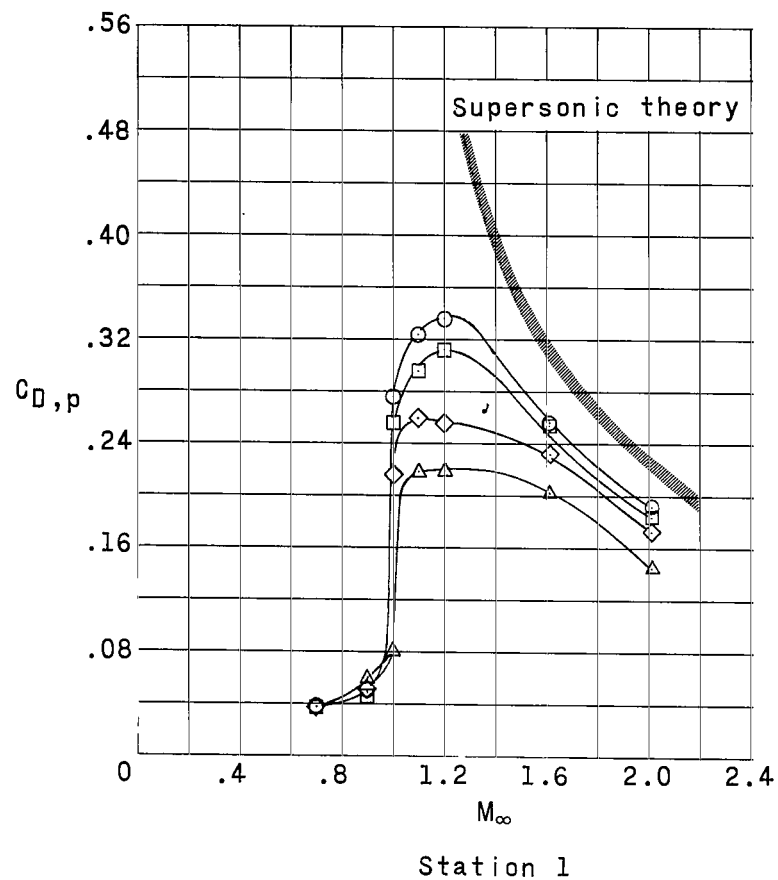


Figure 12.- Variation of pressure-drag coefficient $C_{D,p}$ with M_∞ . Model with 0.053-inch (0.135-cm) protruding waves.

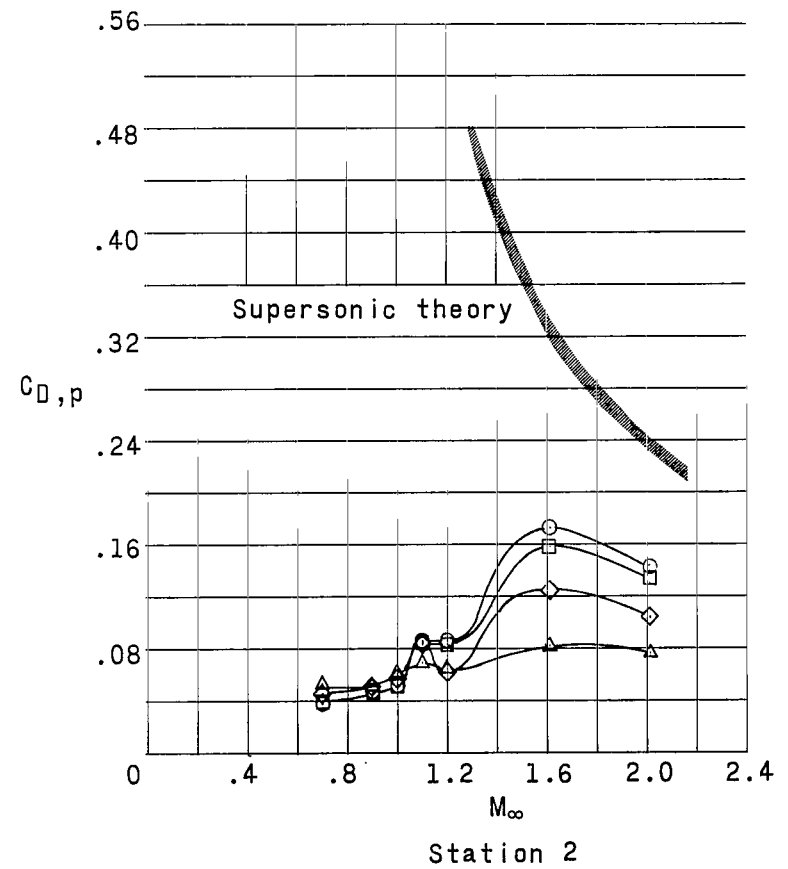
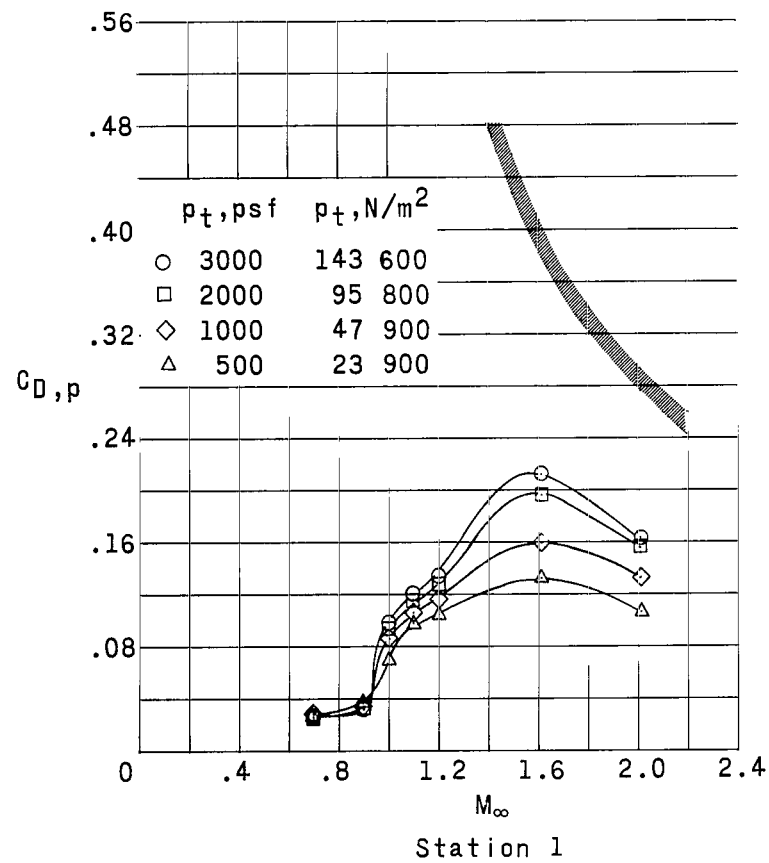


Figure 13.- Variation of pressure-drag coefficient $C_{D,p}$ with M_∞ . Model with 0.053-inch (0.135-cm) transverse creases.

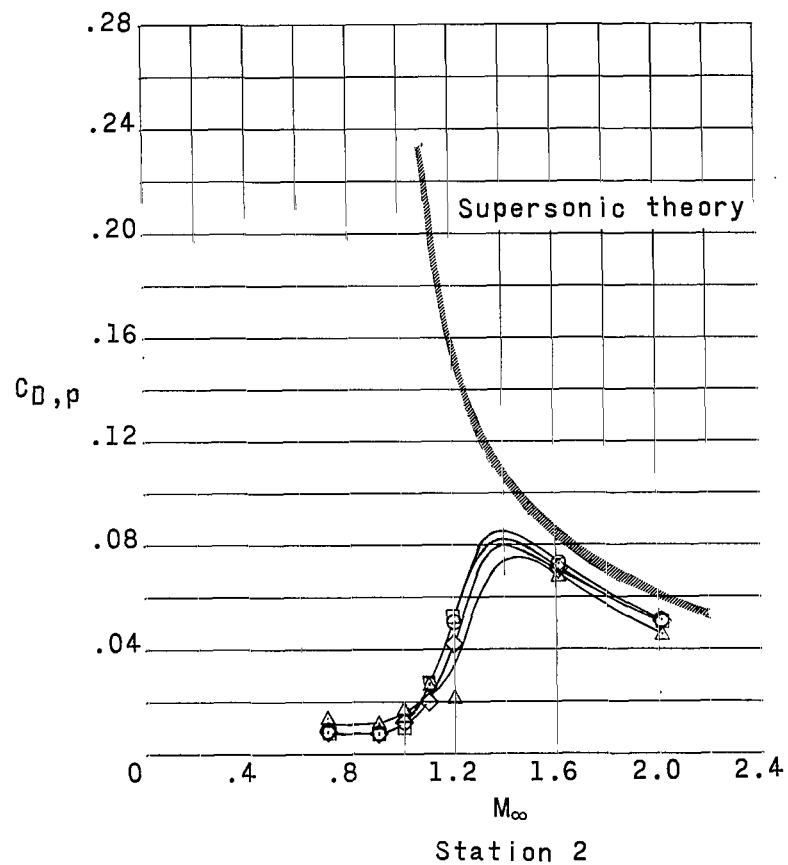
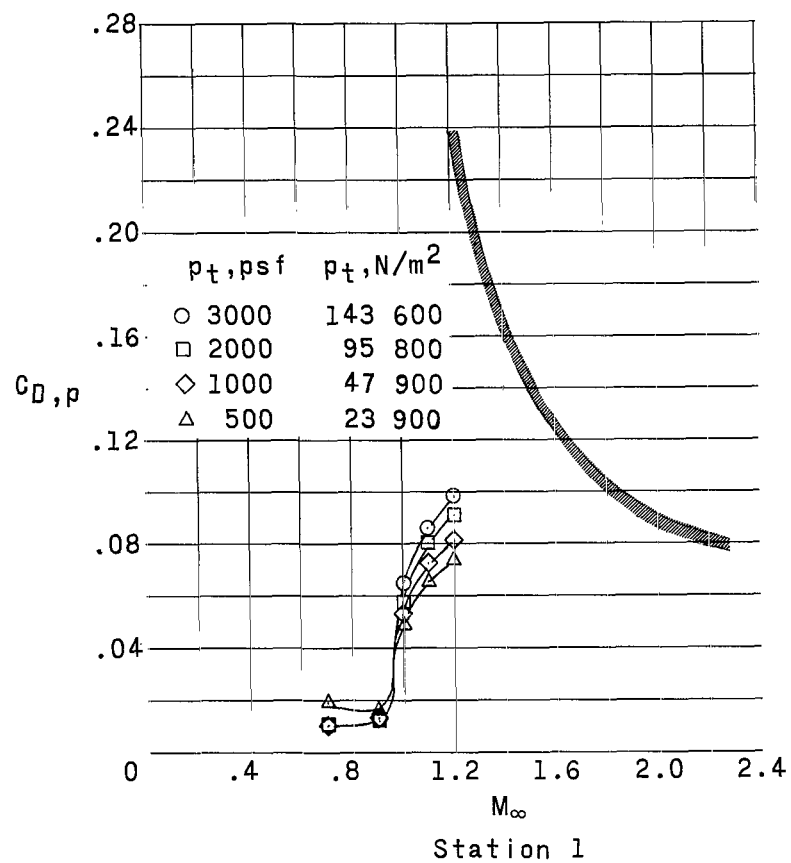


Figure 14.- Variation of pressure-drag coefficient $C_{D,p}$ with M_∞ . Model with 0.017-inch (0.043-cm) transverse creases.

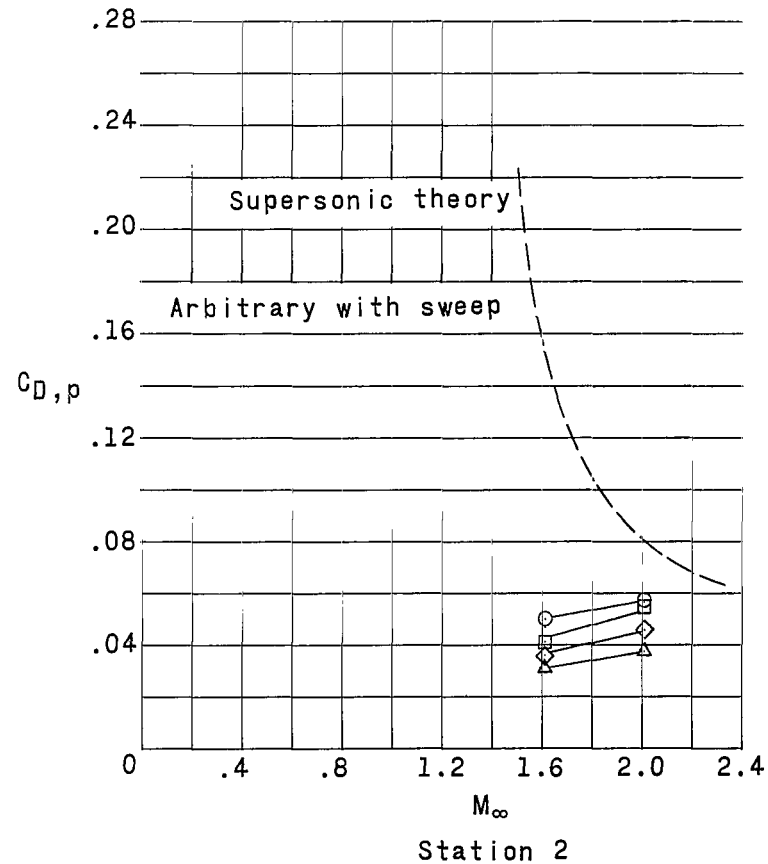
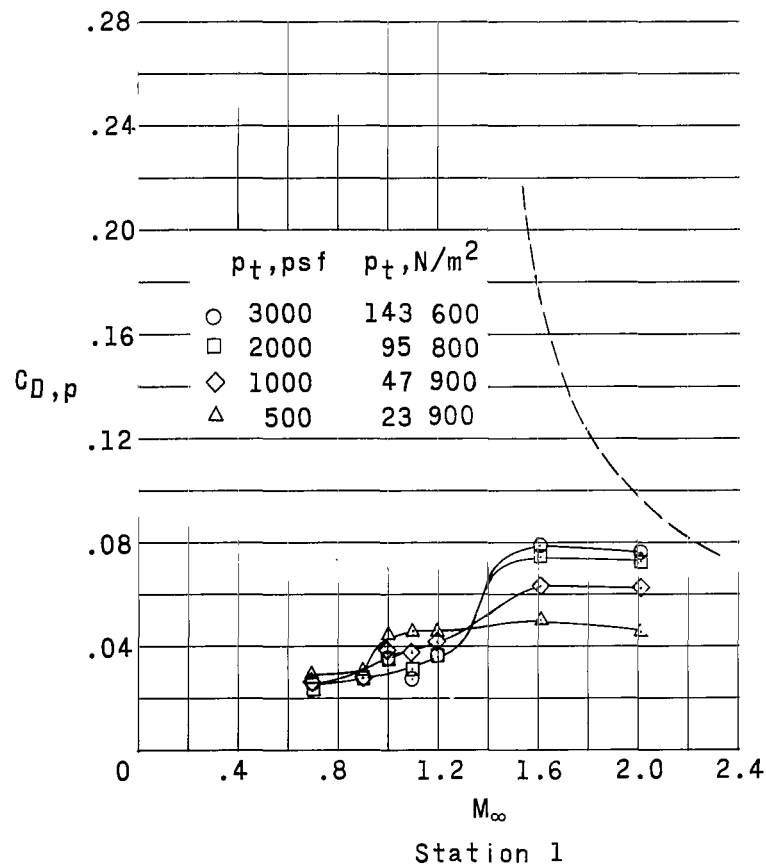


Figure 15.- Variation of pressure-drag coefficient $C_{D,p}$ with M_{∞} . Model with 0.020-inch (0.051-cm) 45° rearward steps.

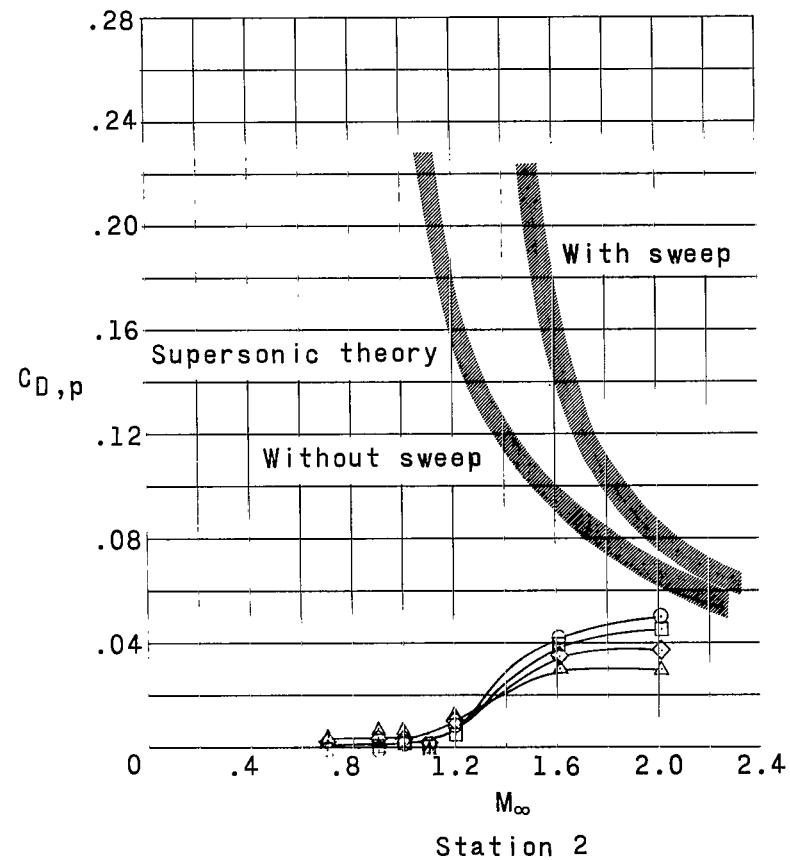
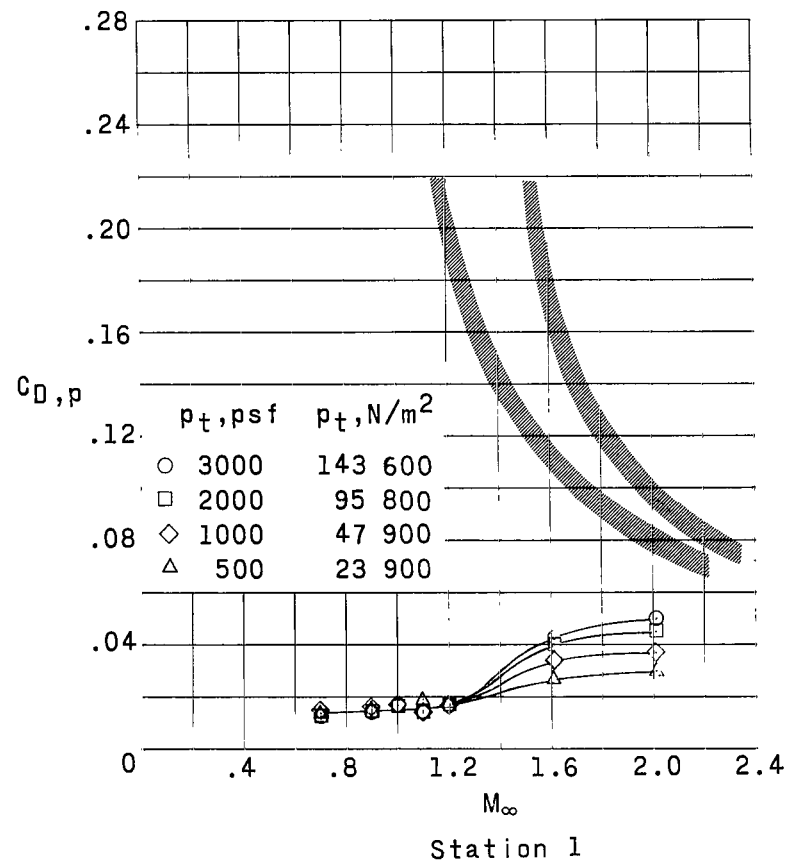


Figure 16.- Variation of pressure-drag coefficient $C_{D,p}$ with M_∞ . Model with 0.014-inch (0.036-cm) 45° creases.

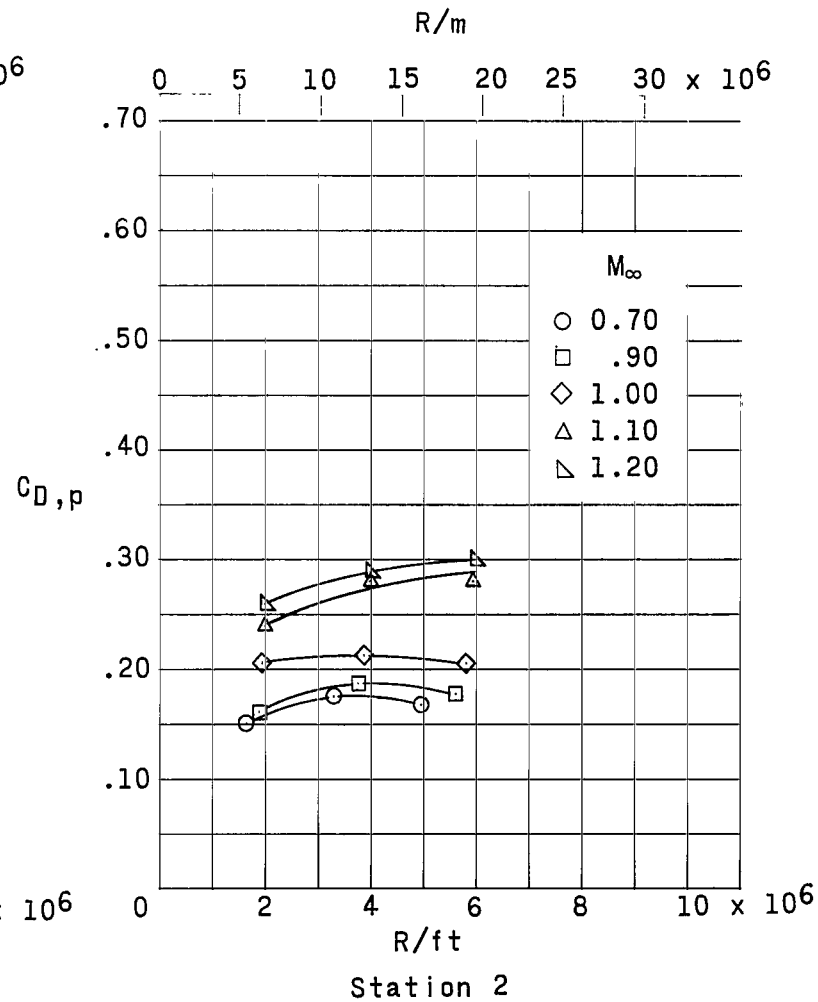
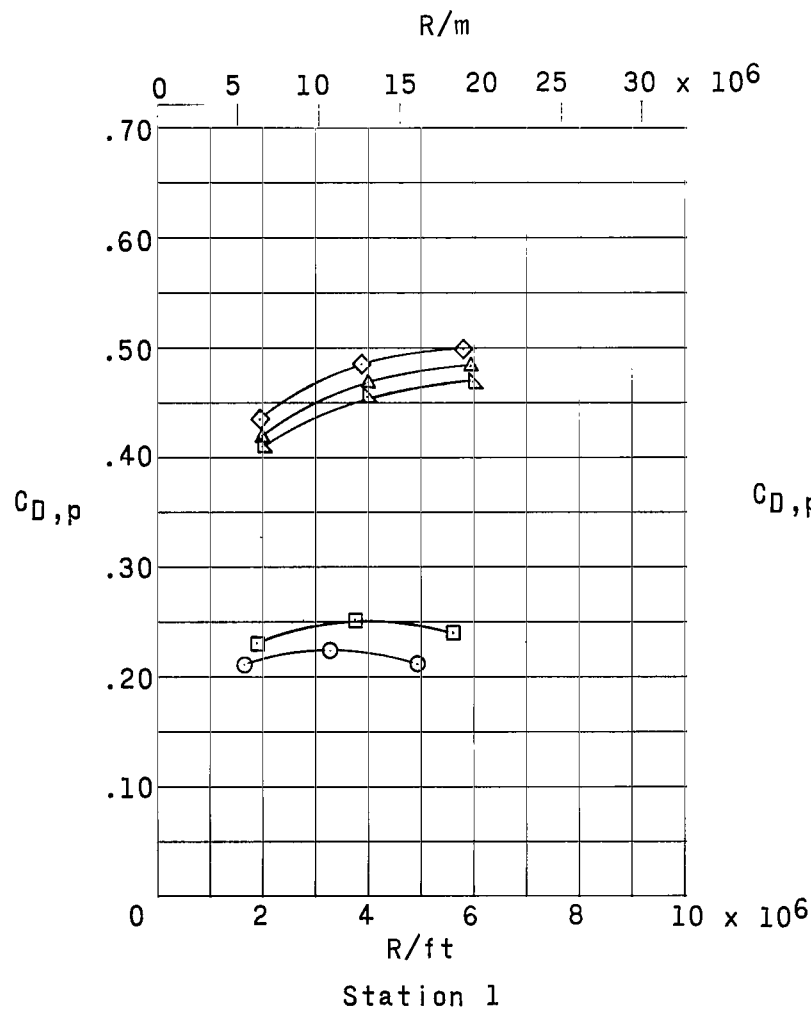


Figure 17.- Variation of pressure-drag coefficient $C_{D,p}$ with R/ft (R/m). Model with 0.021-inch (0.053-cm) steps with grooves.

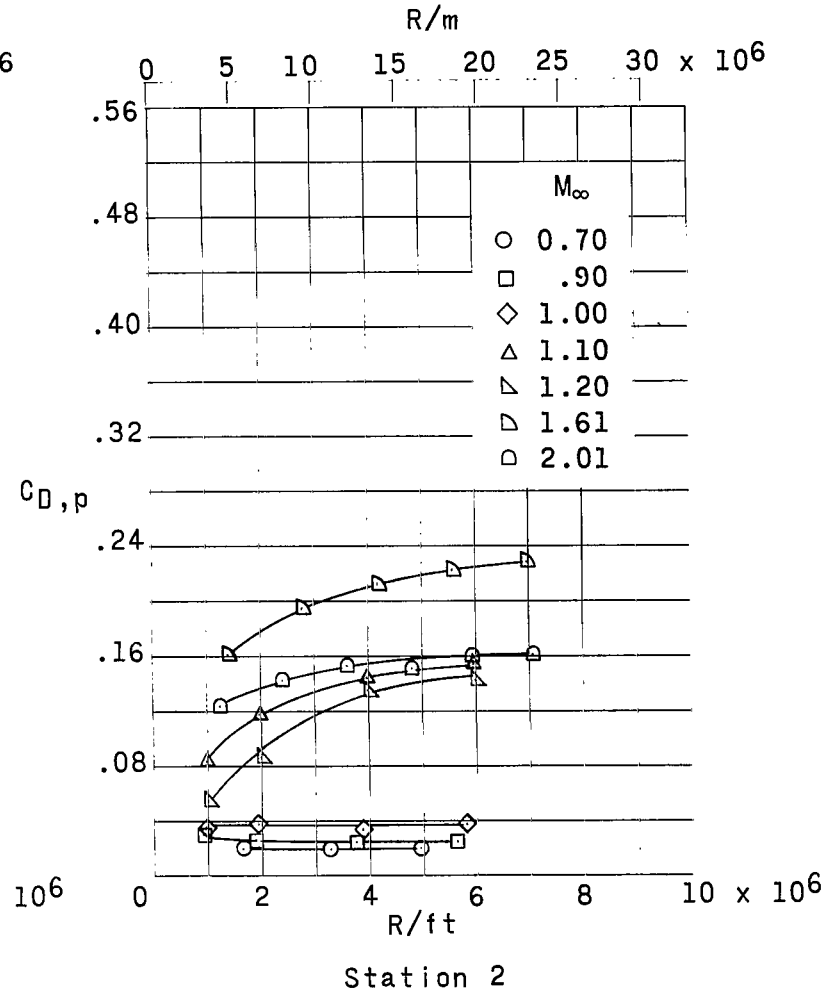
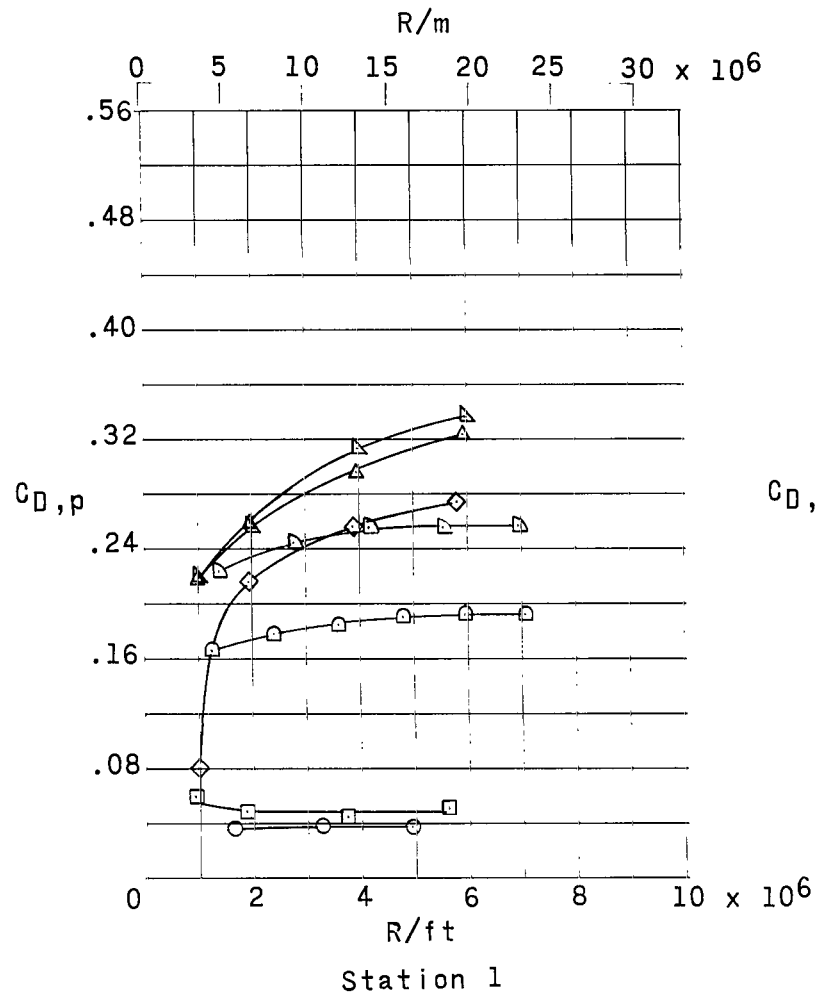


Figure 18.- Variation of pressure-drag coefficient $C_{D,p}$ with R/ft (R/m). Model with 0.053-inch (0.135-cm) protruding waves.

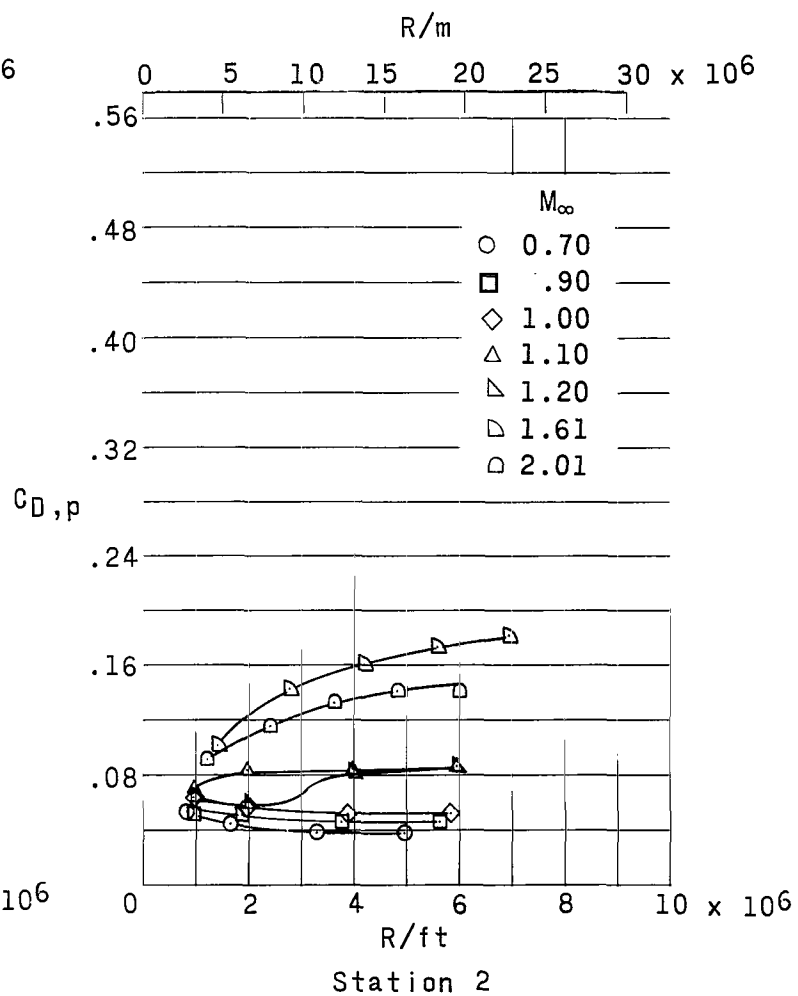
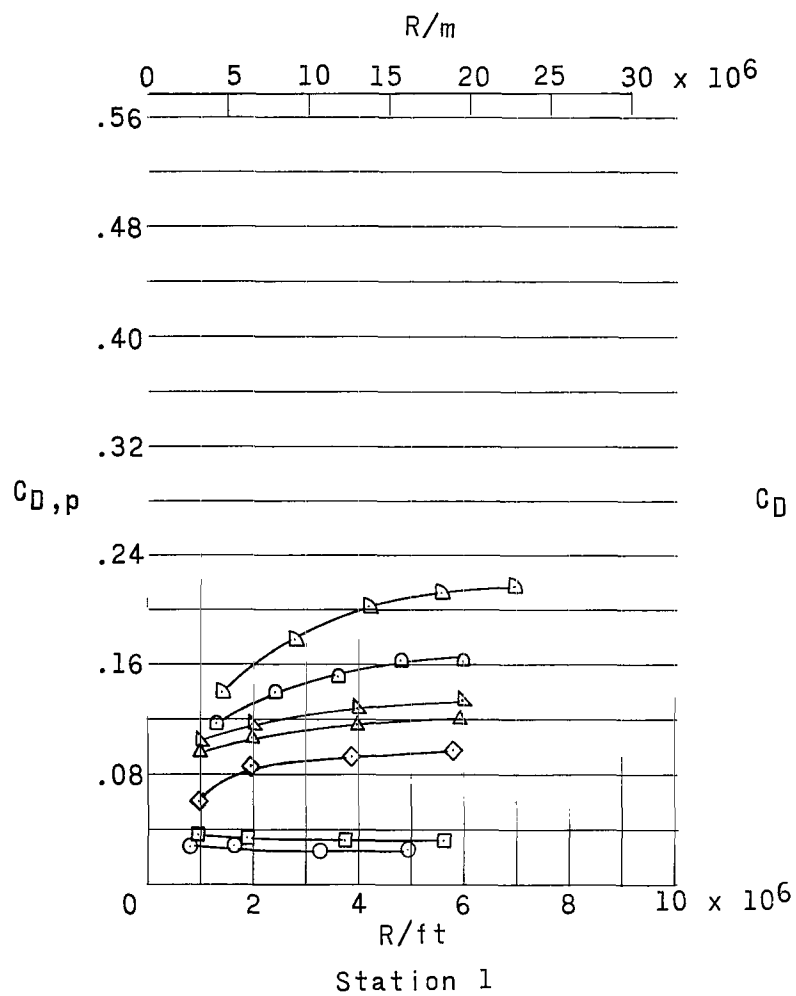


Figure 19.- Variation of pressure-drag coefficient $C_{D,p}$ with R/ft (R/m). Model with 0.053-inch (0.135-cm) transverse creases.

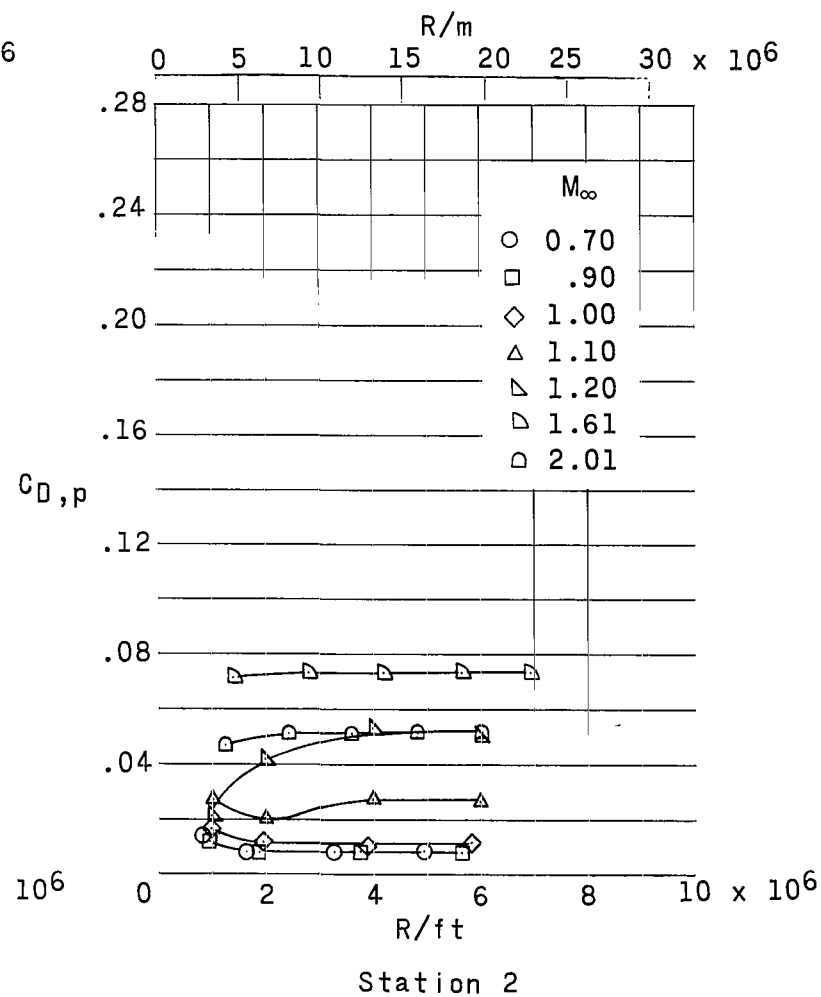
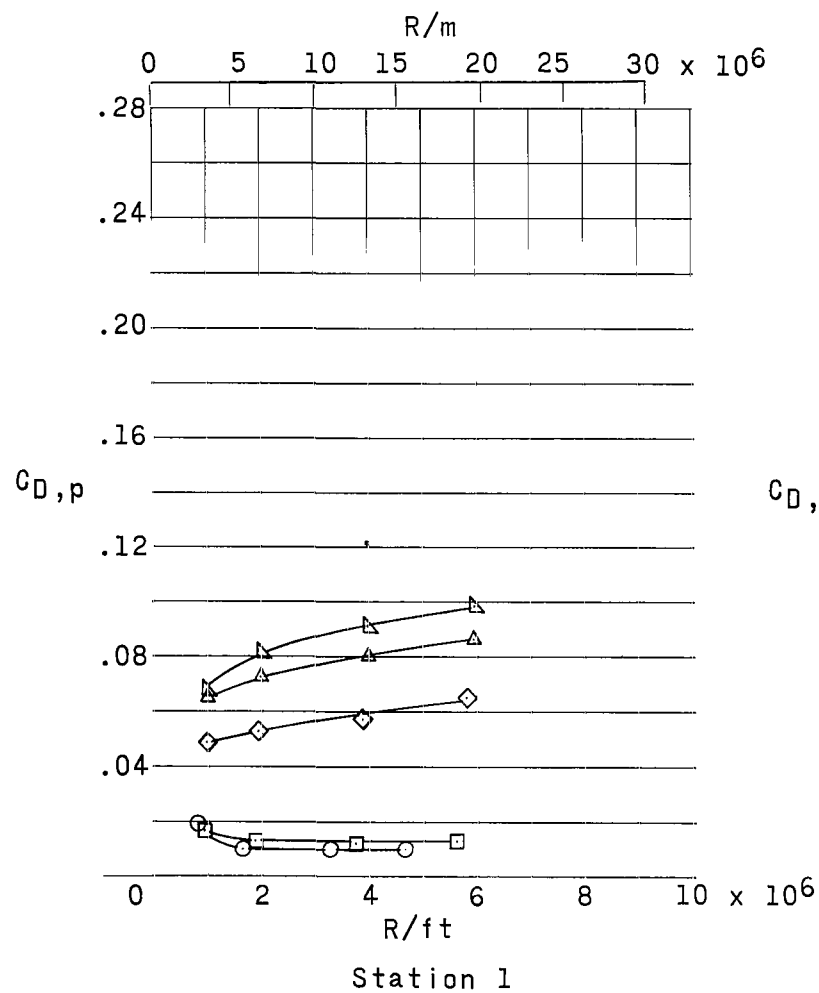


Figure 20.- Variation of pressure-drag coefficient $C_{D,p}$ with R/ft (R/m). Model with 0.017-inch (0.043-cm) transverse creases.

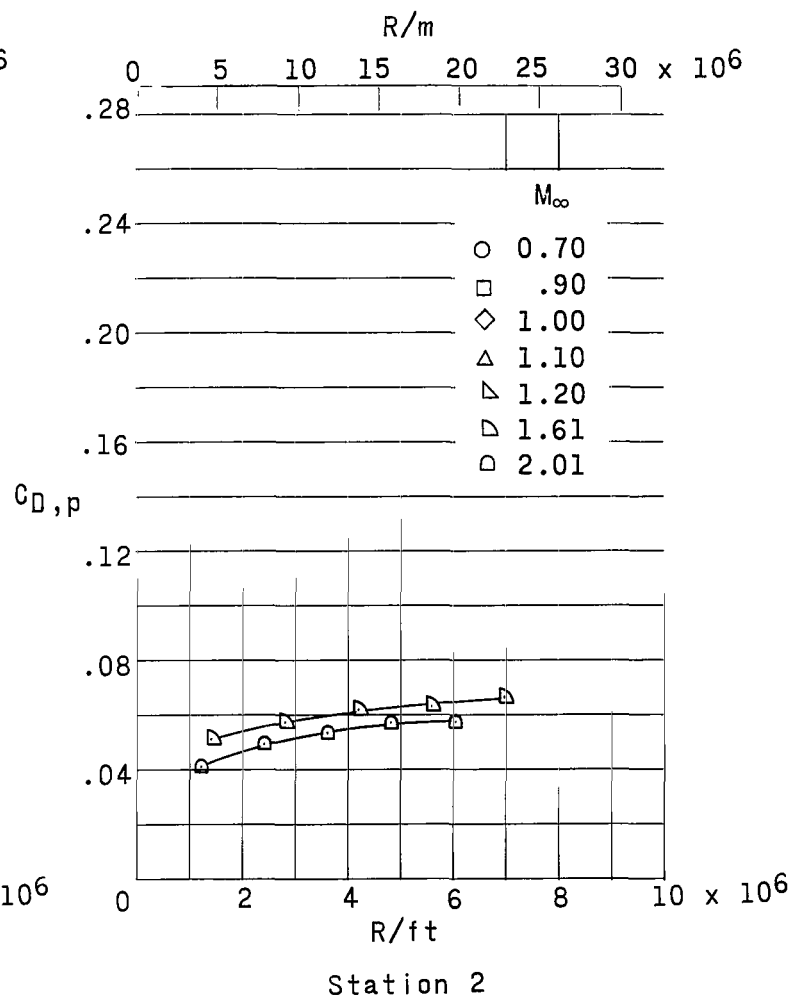
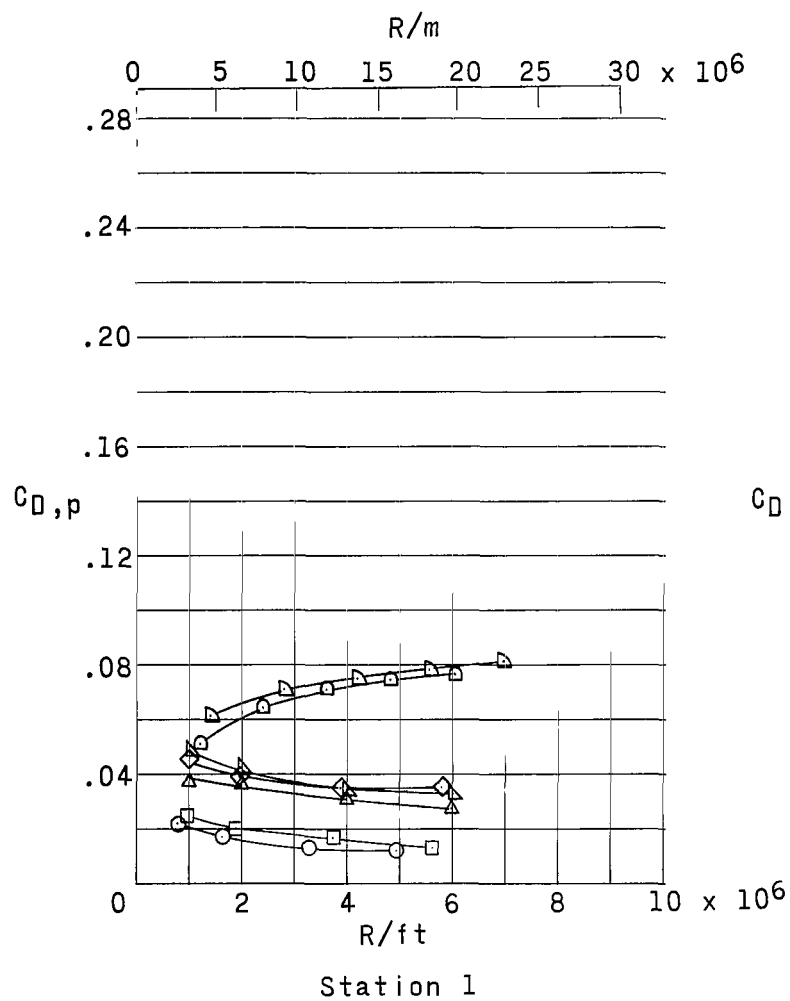


Figure 21.- Variation of pressure-drag coefficient $C_{D,p}$ with R/ft (R/m). Model with 0.020-inch (0.051-cm) 45° rearward steps.

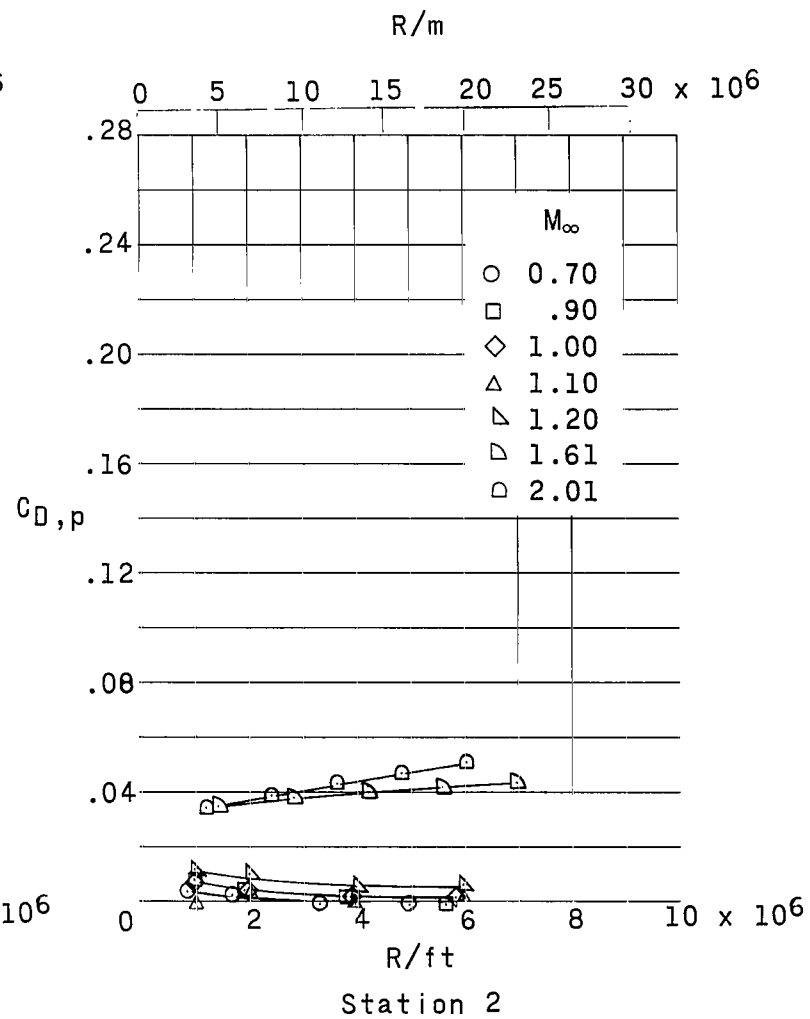
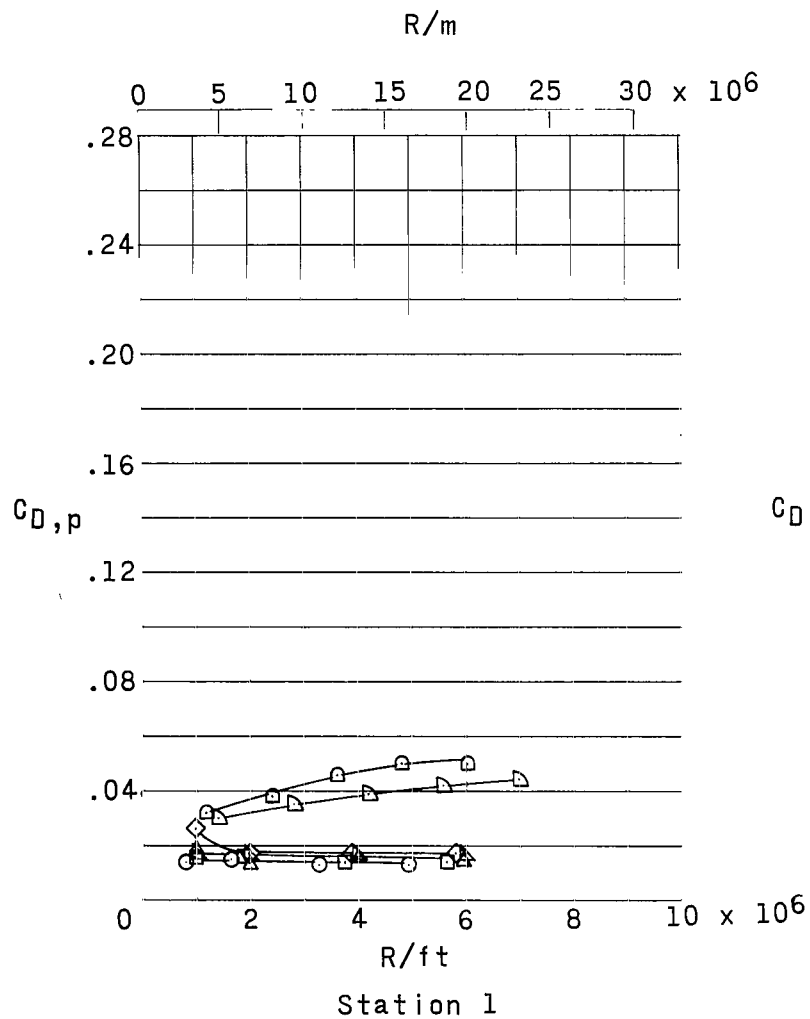


Figure 22.- Variation of pressure-drag coefficient $C_{D,p}$ with R/ft (R/m). Model with 0.014-inch (0.036-cm) 45° creases.

"The aeronautical and space activities of the United States shall be conducted so as to contribute . . . to the expansion of human knowledge of phenomena in the atmosphere and space. The Administration shall provide for the widest practicable and appropriate dissemination of information concerning its activities and the results thereof."

—NATIONAL AERONAUTICS AND SPACE ACT OF 1958

NASA SCIENTIFIC AND TECHNICAL PUBLICATIONS

TECHNICAL REPORTS: Scientific and technical information considered important, complete, and a lasting contribution to existing knowledge.

TECHNICAL NOTES: Information less broad in scope but nevertheless of importance as a contribution to existing knowledge.

TECHNICAL MEMORANDUMS: Information receiving limited distribution because of preliminary data, security classification, or other reasons.

CONTRACTOR REPORTS: Technical information generated in connection with a NASA contract or grant and released under NASA auspices.

TECHNICAL TRANSLATIONS: Information published in a foreign language considered to merit NASA distribution in English.

TECHNICAL REPRINTS: Information derived from NASA activities and initially published in the form of journal articles.

SPECIAL PUBLICATIONS: Information derived from or of value to NASA activities but not necessarily reporting the results of individual NASA-programmed scientific efforts. Publications include conference proceedings, monographs, data compilations, handbooks, sourcebooks, and special bibliographies.

Details on the availability of these publications may be obtained from:

SCIENTIFIC AND TECHNICAL INFORMATION DIVISION
NATIONAL AERONAUTICS AND SPACE ADMINISTRATION
Washington, D.C. 20546